Matching high resolution satellite data and flux tower footprints improves their agreement in photosynthesis estimates

Juwon Kong[a,b], Youngryel Ryu[a,b,c,d*], Jiangong Liu[d], Ben Dechant[d,e,f], Camilo Rey-Sanchez[g,h], Robert Shortt[g], Daphne Szutu[g], Joe Verfaillie[g], Rasmus Houborg[i], Dennis Baldocchi[g]

a Interdisciplinary Program in Landscape Architecture, Seoul National University, Seoul, Republic of Korea

b Integrated Major in Smart City Global Convergence, Seoul National University, Seoul, Republic of Korea

c Department of Landscape Architecture and Rural Systems Engineering, Seoul National University, Seoul, Republic of Korea

d Research Institute of Agriculture and Life Sciences, Seoul National University, Seoul, Republic of Korea

e German Centre for Integrative Biodiversity Research (iDiv), Halle-Jena-Leipzig, Leipzig, Germany

f Leipzig University, Leipzig, Germany

g Department of Environmental Science, Policy and Management, University of California, Berkeley, CA, USA

h Department of Marine Earth, and Atmospheric Sciences. North Carolina State University. Raleigh, NC, USA

i Planet Labs, San Francisco, CA, USA

Keywords: Near-infrared radiation reflected from vegetation; NIRvP; Photosynthesis; Eddy covariance; Footprint; CubeSat,

* corresponding author: Youngryel Ryu (yryu@snu.ac.kr)

Abstract

Mapping canopy photosynthesis in both high spatial and temporal resolution is essential for carbon cycle monitoring in heterogeneous areas. However, well established satellites in sun-synchronous orbits such as Sentinel-2, Landsat and MODIS can only provide either high spatial or high temporal resolution but not both. Recently established CubeSat satellite constellations have created an opportunity to overcome this resolution trade-off. In particular, Planet Fusion allows full utilization of the CubeSat data resolution and coverage while maintaining high radiometric quality. In this study, we used the Planet Fusion surface reflectance product to calculate daily, 3-m resolution, gap-free maps of the near-infrared radiation reflected from vegetation (NIRvP). We then evaluated the performance of these NIRvP maps for estimating canopy photosynthesis by comparing with data from a flux tower network in Sacramento-San Joaquin Delta, California, USA. Overall, NIRvP maps captured temporal variations in canopy photosynthesis of individual sites, despite changes in water extent in the wetlands and frequent mowing in the crop fields. When combining data from all sites, however, we found that robust agreement between NIRvP maps and canopy photosynthesis could only be achieved when matching NIRvP maps to the flux tower footprints. In this case of matched footprints, NIRvP maps showed considerably better performance than *in situ* NIRvP in estimating canopy photosynthesis both for daily sum and data around the time of satellite overpass ($R^2 = 0.78$ vs. 0.60, for maps vs. *in situ* for the satellite overpass time case). This difference in performance was mostly due to the higher degree of consistency in slopes of NIRvP-canopy photosynthesis relationships across the study sites for flux tower footprint-matched maps. Our results show the importance of matching satellite observations to the flux tower footprint and demonstrate the potential of CubeSat constellation imagery to monitor canopy photosynthesis remotely at high spatio-temporal resolution.

1. Introduction

Being able to estimate terrestrial gross primary productivity (GPP) accurately with remote sensing techniques is important for monitoring climate change effects, vegetation responses to environmental extremes and agricultural applications, among other uses. Apart from the chosen approach to estimate GPP from remote sensing variables, the spatial and temporal resolution of the data are important. High spatial resolution satellite data are needed for agricultural applications and monitoring of heterogeneous natural ecosystems. For example, small-scale agricultural fields, which can be fine scale heterogeneous ecosystems, require spatial GPP details to distinguish boundaries between fields and to understand sub-field variation in crop growth (Duveiller and Defourny, 2010; Houborg and McCabe, 2016; Kimm et al., 2020). High temporal resolution is also important within short periods during transition season or extreme environmental events such as droughts.

High spatio-temporal resolution of satellite imagery is not only important to monitor vegetation, it is also crucial for the validation of remote sensing-based GPP products with flux tower measurements (Chen et al., 2011; Ran et al., 2016). While the footprint of eddy covariance flux towers covers a relatively large area (more than 1 km^2 for 80 % cumulative contribution of fluxes) (Chen et al., 2009; Chen et al., 2012), its location, size and shape change continuously, driven by surface roughness and meteorological factors such as wind direction and speed (Kljun et al., 2015; Prabha et al., 2008; Schmid, 1997). Although footprint variations can affect the feasibility to match flux tower GPP with satellite products in any type of ecosystem due to spatial heterogeneity within the flux tower footprint (Giannico et al., 2018), it is a key factor in heterogeneous landscapes as contributions to the tower GPP can come from different land cover types (Ran et al., 2016). Due to the limitations in the spatial resolution of available satellite imagery, this aspect of flux tower footprint shape, size and dynamics has mostly been circumvented by selecting only flux tower sites within large patches of relatively homogeneous ecosystems (Liang et al., 2019; Zhang et al., 2020). Even in such cases of consistent land cover within the flux tower footprint, however, the assumption of spatial homogeneity of GPP within the flux tower footprint might not be justified. An important aspect related to this is that even for tower-based, near-surface sensing techniques, covering the entire flux tower footprint with tower-based optical sensors is virtually impossible even when a bi-hemispheric viewing geometry is used (Gamon, 2015; Liu et al., 2017; Marcolla and Cescatti, 2018).

Remotely monitoring GPP at both high spatial and temporal resolution has been challenging due to the trade-off between spatial and temporal resolutions in observations from sun-synchronous satellites. Most publicly available satellite-derived surface reflectance products, therefore, have either coarse spatial resolution (e.g., 250 m – 1 km) with high revisit frequency (e.g., one day for Moderate Resolution Imaging Spectrometer; MODIS) (Justice et al., 1998) or fine spatial resolution (e.g., 10 m – 30 m) with revisit frequency (e.g., up to 16 days for Sentinel 2 and Landsat 8)(Claverie et al., 2018; Drusch et al., 2012; Roy et al., 2014), which can effectively result in much lower temporal resolution

in many areas due to frequent cloud cover. While many image fusion techniques have been developed (Zhu et al., 2018) and rather successfully applied to partly overcome the trade-off between spatial and temporal resolutions, these approaches still have important limitations. For example, forcing data with a coarse spatial resolution can result in bias against ground measurements, especially in heterogeneous landscapes (Kong et al., 2021).

A recent solution to spatiotemporal trade-offs in satellite observations have been satellite constellations, which consist of a high number of, typically small satellites (i.e., CubeSat; (https://www.cubesat.org/)). CubseSat consists of multiple cubic units (1 unit = 10 cm × 10 cm × 10 cm) but weights, less than 1.33kg unit^{-1}. On the other hand, it introduces another challenge of cross-calibration between a large number of sensors. The Cubesat-enabled Spatio-Temporal Enhancement Method (CESTEM) overcomes the challenges of low radiometric quality and cross-sensor inconsistency among CubeSat images by radiometric normalization using satellite images from rigorously calibrated sensors (Helder et al., 2020; Houborg and McCabe, 2018a). Indeed, CESTEM outperformed other image fusion products in capturing spatial and temporal variation in an *in situ* NDVI dataset for a heterogeneous rice paddy landscape (Kong et al., 2021) and has shown great potential for agricultural applications (Aragon et al., 2018; Aragon et al., 2021; Houborg and McCabe, 2018b). Moreover, Planet Fusion, which is based on CESTEM algorithm, conducts both inter-sensor radiometric harmonization and gap-filling process to deliver daily cloud-free 4-band (blue, green, red, and near infrared; NIR) surface reflectance data with 3 m resolution (Planet Fusion Team, 2021).

Recently, NIR radiation reflected from vegetation has shown promising results in terms of estimating GPP at the field scale of a diverse range of vegetation types (Baldocchi et al., 2020; Dechant et al., 2022; Dechant et al., 2020). NIR reflectance from vegetation is approximated using the NIRv index as the product of the normalized difference vegetation index (NDVI) and NIR reflectance (Badgley et al., 2017). It accurately estimates monthly and annual GPP variations over globally distributed flux tower sites (Badgley et al., 2019). However, reflectance does not include information regarding the amount of incoming photosynthetically active radiation (PAR), which is a dominant factor driving daily GPP variation. Therefore, NIR radiation reflected from vegetation (NIRvP), which is the product of NIRv and PAR, has been proposed as a structural proxy for GPP estimation (Dechant et al., 2022; Dechant et al., 2020; Wu et al., 2020) and has been widely applied at hourly to daily timescales for site-level and larger scale of GPP estimation since then (Baldocchi et al., 2020, 2022; Dechant et al., 2020; Jiang et al., 2021; Liu et al., 2020).

Baldocchi et al. (2020) found that NIRvP from *in situ* spectral sensors tracked diurnal to seasonal variations of tower-based GPP well for individual sites, but that the slopes in the NIRvP-GPP regressions varied considerably across sites and years. As the study of Baldocchi et al. (2020) included spatially heterogeneous sites such as wetlands with considerable variation in water extent and cropland with frequent mowing, the variation in regression slopes could at least partly be due to the footprint mismatch between spectral sensors and eddy covariance systems on the flux towers. This aspect is

explored in detail in our study by generating daily, 3 m GPP maps from CubeSat NIRvP and considering different scenarios to link the satellite-based GPP to the tower observations. In particular, we attempted to answer the following scientific questions:

(i) Does matching daily flux tower footprints with high resolution (3 m) NIRvP improve correlation to GPP compared to a larger fixed area around the tower and *in situ* spectral measurements?

(ii) How do the spatial and temporal resolution of satellite data impact the relationship between NIRvP and GPP when matching the flux tower footprint?

2. Methods

2.1 Study sites

To evaluate Planet Fusion-based GPP estimates, , we selected study wetland and crop sites that had in situ measure measurements of NIRvP in the Sacramento–San Joaquin River delta in California, USA (Figure 1), which are registered in AmeriFlux and FLUXNET (Baldocchi et al., 2001; Pastorello et al., 2020). The five study sites included three restored wetlands (US-Tw4, US-Myb, and US-Snf) and two crop fields (US-Bi1 and US-Bi2 which are alfalfa and corn, respectively), located on Sherman, Bouldin, and Twitchell Islands (Table 1). Ideal conditions for eddy covariance measurements include a homogenous and flat landscape and few disturbances, which is physically impossible in the real world (Chu et al., 2021). For example, the wetland sites had a complex mosaic of water and vegetation. The alfalfa site underwent repeated cuttings and regrowth over an annual course. The corn site had a short growing season, and was plowed and flooded for a period during the year Moreover, the summer growing season is mostly cloud free, hence a suitable venue for evaluating satellite products.US-Bi1 (Rey-Sanchez et al., 2021b) (Alfalfa) is an alfalfa field (*Medicago sativa* L., a C3 plant), which is harvested five to seven times per year and periodically grazed with sheep (Rey-Sanchez et al., 2021c); US-Bi2 (Rey-Sanchez et al., 2021a) (Corn) is a corn field (*Zea mays* L., a C4 plant), which is harvested once per year and flooded in the winter. Two of the wetlands were restored from other land uses over the past decade. US-Myb (Matthes et al., 2021) (Palustrine wetland) was restored from a livestock pasture in 2010 and US-Tw4 (Eichelmann et al., 2021) (Freshwater wetland) was restored from a cornfield in 2013; both sites have heterogeneous bathymetry (Chamberlain et al., 2018). The dominant vegetation in US-Myb and US-Tw4 is a mixture of tules (*Schoenoplectus acutus*, a C3 plant) and cattails (*Typha spp*, a C3 plant) in shallow water (water table depth < 40 cm) (Eichelmann et al., 2018; Valach et al., 2021). US-Snf (Kusak et al., 2020) (Pasture) is a wetland, more specifically peatland (Kasak et al., 2021) and is also used as a pasture to graze cattle throughout the seasons. The peak growing season over pasture site was around December to June. All study sites are registered with the AmeriFlux Network with publicly available data (Hemes et al., 2019).

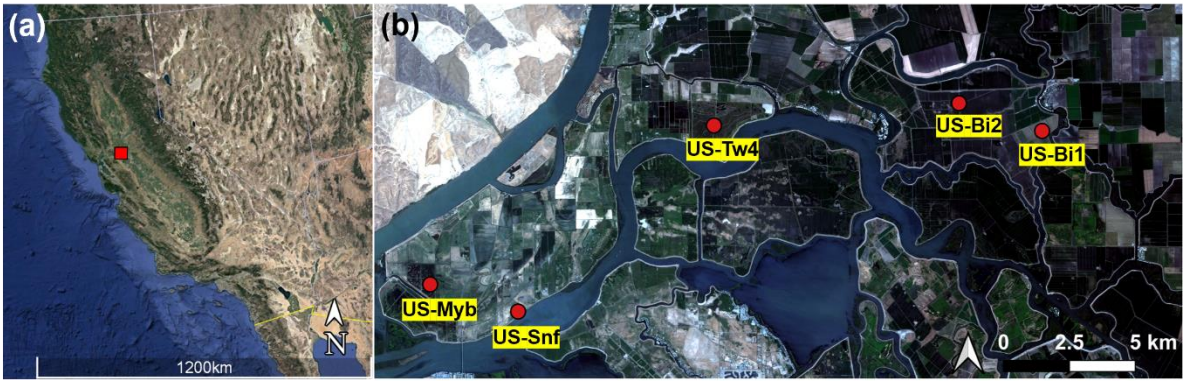

Figure 1 Maps of the study sites. (a) A map of California. (Image source: Google Earth) with the location of Sacramento–San Joaquin River delta area indicated by the red square. (b) The Sacramento–San Joaquin River delta area with red points that indicate study sites. Image source: red–green–blue (RGB) Planet Fusion surface reflectance product for July 1, 2018 (resolution, 3 m; projection, WGS84/UTM zone 10N; area, 30.6 km × 14.2 km = 433 km^2).

Table 1 List of study sites. Latitude and longitude of the flux tower (projection, WGS84) were adjusted from sub-meter spatial resolution satellite images from Google Earth and confirmed by field visits (Figure S1). The normalized difference vegetation index (NDVI) sensor position indicates distances (m) from the flux tower to the east and north, as well as height.

Site name (Site ID) DOI for citation	**Type**	**Typical vegetation**	**Study period**	**Latitude, Longitude** **NDVI sensor position**
Bouldin Alfalfa (US-Bi1) https://doi.org/10.17190/AMF/1480317	Crop (Alfalfa)	Medicago sativa L. (Hemes et al., 2019)	2018-01-01 to 2018-12-31	38.099161, -121.499336 2.89, -2.78, 2.7
Bouldin Corn (US-Bi2) https://doi.org/10.17190/AMF/1419513	Crop (Corn)	Zea mays (Knox et al., 2015)	2018-01-01 to 2018-12-31	38.109078, -121.535122 -2.03, -1.94, 4.42
Twitchell Wetland East End (US-Tw4) https://doi.org/10.17190/AMF/1246151	Wetland	Schoenoplectus acutus & Typha spp. (Hemes et al., 2020)	2018-01-01 to 2018-12-31	38.102747, -121.641325 -2.17, -1.73, 4.73
Mayberry (US-Myb) https://doi.org/10.17190/AMF/1246139	Wetland	Schoenoplectus acutus & Typha spp (Eichelmann et al., 2018)	2019-01-01 to 2019-12-31	38.049864, -121.765006 3.10, 2.3, 4
Sherman Barn (US-Snf) https://doi.org/10.17190/AMF/1579718	Wetland (Pasture)	* Unreported (Kasak et al., 2021)	2019-07-19 to 2019-12-31	38.040208, -121.727161 -1.49, -2.49, 2.75

2.2 *In situ* measurements

To evaluate GPP estimates derived from CubeSat NIRvP maps, we compared them with *in situ* carbon

flux measurements from eddy covariance systems, surface reflectance measurements from NDVI sensors, and quantum sensor PAR measurements.

The eddy covariance systems included open-path infrared gas analyzers (LI-7500A for CO_2 and H_2O, LI-7700 for CH_4; LiCOR Inc., Lincoln, NE, USA), and three-dimensional sonic anemometers (WindMaster Pro 1590, Gill Instruments Ltd, Lymington, Hampshire, UK) that measure sonic temperature and three-dimensional wind speeds at 20 Hz. High-frequency raw data processing and flux computations were performed in accordance with the methods of Pastorello et al. (2020). Briefly, standard processing procedures included spike removal for 20-Hz raw data, coordinate rotations within each 30-min block for anemometer tilt correction, block averaging for 30-min fluxes of net ecosystem CO_2 exchange (NEE), air density corrections and site-specific friction velocity filtering. Furthermore, we applied a neural network procedure (Moffat et al., 2007) to fill the gaps in 30-min NEE time series and then partitioned NEE into ecosystem assimilation and ecosystem respiration flux densities using the nighttime approach (Reichstein et al., 2005). A detailed description about flux data processing, gap-filling and partitioning can be found in Eichelmann et al. (2018) and Knox et al. (2015). The proportion of gap-filled GPP at each site during the study period was 36.8 % (US-Bi1; Alfalfa), 27.6 % (US-Bi2; Corn), 25.2 % (US-Tw4; Freshwater wetland), 27.0 % (US-Myb; Palustrine wetland), and 25.3 % (US-Snf; Pasture).

.

In situ NIRv data were derived from NDVI sensors (Decagon SRS-Ni, Pullman, WA, USA) that measured incident and reflected radiation in the red (630 nm; full-width, half-maximum, 50 nm) and NIR (800 nm; full-width, half-maximum, 40 nm) spectral bands. NDVI sensors were mounted on booms extended from the flux tower (Table 1). We measured bi-hemispheric reflectance by using hemispherical view for both upward and downward looking sensors to increase the area of the footprint viewed by the NDVI sensors (Baldocchi et al., 2020). Although the field of view of the NDVI sensors with bi-hemispheric view include the tower structure, this is expected to be a small, and temporally constant bias. In particular, the NDVI of the tower structure elements is expected to be very low, effectively decreasing the contribution to NIRv. Planet Fusion (Section 2.3) provides a bidirectional reflectance factor that differs from bi-hemispheric reflectance; therefore, we tested the impacts of the different reflectance quantities on NIRv over two study sites using satellite-derived bidirectional reflectance distribution function (BRDF) parameters and the result demonstrated a negligible difference (Figure A1). Moreover, radiometric calibration had been done for each NDVI sensor before and after the growing season but slow drift year after year in NDVI sensor over the site (US-Tw4)was not a scope of uncertainty in this study as we only used single year data. At each tower, *in situ* incoming PAR data ($\mu mol\ m^{-2}\ s^{-1}$) were measured by quantum sensors (PAR-Lite or PQS1, Kipp & Zonen, Delft, Netherlands).

To align the time between continuous *in situ* measurements and Planet Fusion data that rely on morning to around noon overpass time of satellites such as Sentinel 2 (around 1015hh – 1030hh) and Landsat 8 (around 1015hh – 1030hh), and MODIS nadir BRDF-adjusted reflectance (local solar noon), we averaged *in situ* measurements (i.e., GPP, PAR, and NIRv, hereafter $\mathrm{NIRv}^{\mathrm{in\ situ}}$) between 1030hh. and 1230hh to align it to Planet Fusion data. For daily GPP and *in situ* daily NIRvP (daily $\mathrm{NIRvP}^{\mathrm{in\ situ}}$), we summed half-hourly GPP and half-hourly *in situ* NIRvP over the whole day (0000hh – 2400hh) to obtain daily sum values, respectively.

2.3 Planet Fusion NIRvP

NIRvP was calculated on the basis of Planet Fusion (PF) surface reflectance data (Planet Fusion Team, 2021). Planet Fusion constitutes a comprehensive harmonization and fusion methodology based on the CESTEM algorithm (Houborg and McCabe, 2018a; Houborg and McCabe, 2018b). Planet Fusion performs multi-sensor inter-calibration, harmonization, enhancement, and fusion leveraging rigorously calibrated and freely available datasets from Sentinel-2, Landsat 8, Moderate Resolution Imaging Spectroradiometer (MODIS), and Visible Infrared Imaging Radiometer Suite (VIIRS) in concert with the higher spatial and temporal resolution CubeSat images from the PlanetScope Constellations. Planet Fusion uses the Framework for Operational Radiometric Correction for Environmental Monitoring (FORCE) (Frantz, 2019) to generate a 30 m harmonized Sentinel-2 and Landsat 8 BRDF adjusted surface reflectance product to be used as the calibration target during the CESTEM-based radiometric harmonization step. In that harmonization step, a cubist rule-based regression technique was used for constructing band-specific prediction models, which were trained by the FORCE-based Sentinel-2 and Landsat 8 surface reflectance product (30 m) and aggregated-PlanetScope data (30 m). Further details on the original CESTEM methodology are in Houborg and McCabe (2018a). Additional Planet Fusion features include 1) sub-pixel fine geometric alignment of source imagery, 2) rigorous, temporally driven, cloud and cloud shadow detection to remove the cloud-related pixels, 3) fusion of Sentinel-2 and Landsat 8 data to help fill gaps in PlanetScope coverage, and 4) advanced gap-filling (Planet Fusion Team, 2021). Planet Fusion delivers daily, gap-filled, 4-band (0.45 – 0.51 µm, blue; 0.53 – 0.59 µm, green; 0.64 – 0.67 µm, red; 0.85 - 0.88 µm, NIR) sensor agnostic surface reflectance data characterized by enhanced radiometric stability and consistency across space and time to support advanced analytics. Planet Fusion product isgenerated with a 3 m pixel size as regularly gridded raster tiles (24 by 24 km) in UTM projection. In this study, Planet Fusion data were provided for the years 2018 and 2019 by utilizing Harmonized Landsat and Sentinel (referred to as HLS from hereon) (Claverie et al., 2018) as the calibration target, which is different from the currently available Planet Fusion product that uses FORCE-based Sentinel-2 and Landsat surface reflectance product.

To calculate instantaneous Planet Fusion -based NIRvP, we used NIRv maps from Planet Fusion data

and PAR from tower-based quantum sensors located at the sites. First, we calculated NDVI maps using Planet Fusion red and NIR reflectance maps, according to Eq. (1). Then, we multiplied them by NIR reflectance to generate NIRv maps, according to Eq. (2). Finally, we applied Eq. (3) to estimate NIRvP for each site using averaged PAR data collected by *in situ* PAR sensors around satellite overpass time. Although Planet Fusion inherits overpass time of Sentinel 2 and Landsat 8 (around 1015hh – 1030hh) in theory, we assumed the time window between 1030hh and 1230hh when aligning it to *in situ* data. MODIS affects the daily variation of Planet Fusion more than Sentinel 2 and Landsat. Specifically, MCD43A4 products (Schaaf et al., 2002), which are forcing data for Planet Fusion, use the data from both MODIS terra (overpass at 1030hh) and MODIS aqua (overpass at 1330hh).

$$\boldsymbol{NDVI} = \frac{\boldsymbol{\rho NIR} - \boldsymbol{\rho Red}}{\boldsymbol{\rho NIR} + \boldsymbol{\rho Red}} \quad \text{Eq. (1)}$$

$$\boldsymbol{NIRv} = \boldsymbol{\rho NIR} \times \boldsymbol{NDVI} \quad \text{Eq. (2)}$$

$$\boldsymbol{NIRvP} = \boldsymbol{NIRv} \times \boldsymbol{PAR} \quad \text{Eq. (3)}$$

where ρNIR and ρRed are reflectance in the NIR and red regions, respectively

To generate daily Planet Fusion NIRvP maps, we used both satellite-derived daily summed PAR data and *in situ* PAR data. As Planet Fusion products are snapshots of daytime conditions around satellite overpass time, rather than daily accumulated values, we temporally upscaled Planet Fusion NIRvP around the satellite overpass time to generate daily Planet Fusion NIRvP (daily $\mathrm{NIRvP}^{\mathrm{PF}}_{\mathrm{ECfootprint}}$). This temporal upscaling process successfully upscaled GPP (Ryu et al., 2012), using a simple cosine function computed from the solar zenith angle, latitude, and longitude. For the application of Planet Fusion NIRvP where *in situ* PAR were not available, we multiplied Planet Fusion NIRv with daily summed PAR data (BESS daily PAR, 5 km; daily $\mathrm{PAR}^{\mathrm{BESS}}$) (Ryu et al., 2018), which were retrieved from the satellite-based Breathing Earth System Simulator (BESS) PAR product (Ryu et al., 2011)(Figure 2). The BESS PAR product uses MODIS Terra and Aqua data to upscale available instantaneous PAR estimates into daily summed values by combining an atmospheric radiative transfer model(i.e., Forest Light Environmental Simulator, FLiES; Kobayashi and Iwabuchi (2008)) with an artificial neural network. The daily $\mathrm{PAR}^{\mathrm{BESS}}$data showed a strong linear relationship to daily $\mathrm{PAR}^{in\ situ}$ data with little bias ($R^2 = 0.97$, relative bias = -0.8%) (Figure A2).

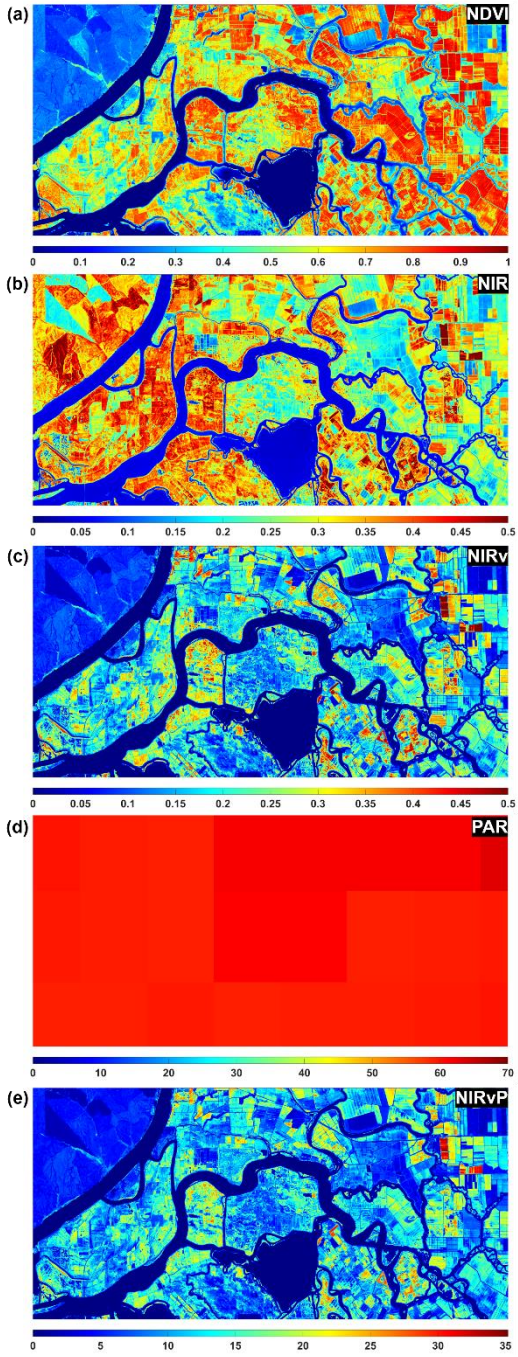

Figure 2 Maps of (a) NDVI, (b) NIR, (c) NIRv, and (d) BESS daily PAR (e) NIRvP derived from the combined Planet Fusion surface reflectance product (3 m resolution) and BESS daily PAR product (5 km resolution) on July 1, 2018 (projection, WGS84/UTM zone 10N; area, 30.6 km × 14.2 km = 433 km^2). NDVI, NIR, and NIRv are given in unitless; PAR and NIRvP are given in unit of mol m^{-2} d^{-1}.NIRvP maps of different times during the year is (Figure S2)

2.4 Flux footprint model

Flux footprints for each of the sites were calculated with the model from Kormann and Meixner (2001). This model outperformed other commonly-used flux footprint models according to a CO_2 gas release experiment (Kumari et al., 2020; Rey-Sanchez et al., in prep). Flux footprints were calculated for those

half hours between 1030hh – 1230hh, and later aggregated at the daily level to produce 50, 60, 70, and 80% footprint contours. An 80% footprint contour indicates that 80% of the sources/sinks contributing to the signal detected by the eddy-covariance tower are located within the indicated area. Multiple contours were calculated to obtain a visual inspection of the exponential decay of the footprint past the 50 % contour line. The 80 % threshold selection is supported by Chu et al. (2021), who found that footprint area beyond the 80% contour had a minimal influence on the final calculations of footprint representativeness in a study of monthly footprint-weight maps.. To obtain highly accurate footprint contours we calculated aerodynamic canopy height using the algorithm of Pennypacker and Baldocchi (2016), which has been shown to track detailed trends in the growth of wetland canopies at our study site (Kasak et al., 2020) and in other sites (Chu et al., 2018). Roughness length and displacement height were calculated as 0.1, and 0.66 of canopy height, respectively.

2.5 Evaluation

We evaluated the performance of the Planet Fusion -derived NIRvP product for GPP estimation by comparing it with *in situ* measurements from both NDVI sensor and eddy covariance system data (Chu et al., 2021). For that, we compared satellite-derived NIRv (and NIRvP) data with *in situ* measurements using several metrics. The coefficient of determination (R^2) of the linear regression between NIRv(P) and GPP, which equals the square of the Pearson correlation coefficient, was used as the main metric to characterize the strength of the linear relationship and thus the GPP estimation performance of NIRv(P). The linear regression slope indicates the variation in the relationship of $NIRv^{PF}$ (or $NIRvP^{PF}$) to GPP for different ecosystem types. Root mean square error (RMSE), bias, and relative bias were calculated as follows:

$$\mathbf{RMSE} = \sqrt{\mathbf{E}((\mathbf{A}-\mathbf{B})^{\mathbf{2}})} \quad \text{Eq. (4)}$$

$$\mathbf{Bias} = \mathbf{E}(\left|\left|\mathbf{B}-\mathbf{A}\right|\right|) \quad \text{Eq. (5)}$$

$$\mathbf{rbias} = \frac{\mathbf{E}(\left|\left|\mathbf{B}-\mathbf{A}\right|\right|)}{\mathbf{E}(\mathbf{A})} \quad \text{Eq. (6)}$$

where A is the satellite product (i.e., MODIS, HLS, or Planet Fusion), B is *in situ* NIRv, and E is the mean operator.

First, we directly evaluated Planet Fusion NIRv against NIRv calculated from *in situ* sensors, which can be considered a direct ground validation. We estimated the footprints of *in situ* NDVI sensors based on their heights and locations (Table 1). Because NDVI sensors measure hemispherical irradiance, we approximate the 80% footprint of *in situ* NIRv from the area of 80% of upwelling irradiance, which can be estimated by considering the sensor height above the ground (Table 1) (Liu et al., 2017). The estimated diameters of the NDVI sensor footprints ($NDVI_{sensor}$) were approximately 12 m (US-Bi1;

Alflafa), 19 m (US-Bi2; Corn), 20 m (US-Tw4; Freshwater wetland), 12 m (US-Snf; Pasture), and 13 m (US-Myb; Palustrine wetland). We designated Harmonized Landsat/Sentinel (HLS) pixels that included $NDVI_{sensor}$ as a footprint type to be considered in the comparison of different approaches, inHLS. Thus, each inHLS footprint contained one (US-Myb; Palustrine wetland) or two HLS pixels (US-Bi1, Alflafa; US-Bi2, Corn; US-Tw4, Freshwater wetland; or US-Snf, Pasture) (Figure 3 and A3). We compared the Planet Fusion NIRv product within the estimated footprint of the NDVI sensors ($NIRv^{PF}_{NDVIsensor}$) and *in situ* NIRv measurements. We extracted HLS pixels covering NDVI sensor footprints (Figure 3 and A3) and extracted Planet Fusion NIRv data within the inHLS footprint ($NIRv^{HLS}_{inHSL}$) to quantify spatial variation in NIRv.

Second, we evaluated Planet Fusion NIRv (and NIRvP) for GPP estimation by comparing it to GPP from the eddy covariance systems. The flux footprint indicates the source area of trace gases detected by an EC system and therefore can be used for pixel selection during CubeSat GPP evaluation. In this study, we used cumulative eddy covariance footprints up to 80% at satellite overpass time for each day (1030hh – 1230hh) ($EC_{footprint}$). When extracting Planet Fusion pixels within the $EC_{footprint}$, we weighted the pixel values based on footprint contribution. We used an 80% accumulated footprint area for the weighting. We split the weighting factors from 0-50%, 50-60%, 60-70% and 70-80% (Eq. (7)).

$$NIRv(P)_{ECfootprint} = \sum_{k=1}^{N}\left(\frac{NIRv_k\ within\ CL_{50\,\%}}{N\ within\ CL_{50\,\%}} \times \frac{50}{80}\right) + \sum_{k=1}^{N}\left(\frac{NIRv_k\ between\ CL_{60\,\%}\ and\ CL_{50\,\%}}{N\ between\ CL_{60\,\%}\ and\ CL_{50\,\%}} \times \frac{60-50}{80}\right) + \sum_{k=1}^{N}\left(\frac{NIRv_k\ between\ CL_{70\,\%}\ and\ CL_{60\,\%}}{N\ between\ CL_{70\,\%}\ and\ CL_{60\,\%}} \times \frac{70-60}{80}\right) + \sum_{k=1}^{N}\left(\frac{NIRv_k\ between\ CL_{80\,\%}\ and\ CL_{70\,\%}}{N\ between\ CL_{80\,\%}\ and\ CL_{70\,\%}} \times \frac{80-70}{80}\right) \quad \text{Eq. (7)}$$

Where k is each pixel number in the total number(N) of pixels within the footprint area, $CL_{D\,\%}$ is D % footprint contour line.

We also chose a fixed 100 m by 100 m area centered on the flux towers (Figure 3; Table 2), which is greater than the footprint of *in situ* NDVI sensor and partly covers the flux tower footprint, . Such fixed footprints have been applied in previous studies because of the use of coarse spatial resolution satellite products (Heinsch et al., 2006; Kim et al., 2006; Verma et al., 2015). We extracted Planet Fusion pixels from the fixed-area footprint (100 m x 100 m)centered on the towers ($NIRv^{PF}_{100m}$) and the estimated footprint area at satellite overpass time for each day ($NIRv^{PF}_{ECfootprint}$). Then, we compared $NIRv^{PF}_{NDVIsensor}$, $NIRv^{PF}_{100m}$, and $NIRv^{PF}_{ECfootprint}$ (and corresponding NIRvP) with GPP estimates around satellite passing time to evaluate the GPP estimation performance of each footprint type. Additionally, we used annual accumulated footprint over Alfalfa (Bi1), Corn (Bi2), and Freshwater wetland (Tw4) (Figure A3) to evaluate the impact of temporal resolution of Planet Fusion NIRvP on GPP estimation. The comparison of Planet Fusion pixels within annual accumulated footprints to GPP is in (Figure A9). We also resampled Planet Fusion data to a 30 m resolution using the nearest-neighbor

interpolation method without antialiasing, which produced the results closest to *in situ* measurements when resampling Planet Fusion-like data from 3 to 30 m resolution (Kong et al., 2021). Next, we extracted pixels within $EC_{footprint}$ to test the effect of spatial resolution on GPP estimation performance by comparison with the original 3 m resolution (Li et al., 2008). Finally, we compared daily $NIRvP^{PF}_{ECfootprint}$ and $NIRv^{PF}_{ECfootprint}$ multiplied by daily PAR^{BESS} against daily GPP. For each footprint type, we extracted pixels only when their centers were within the footprint (poly2mask; MATLAB; The MathWorks, Inc., Natick, MA, USA).

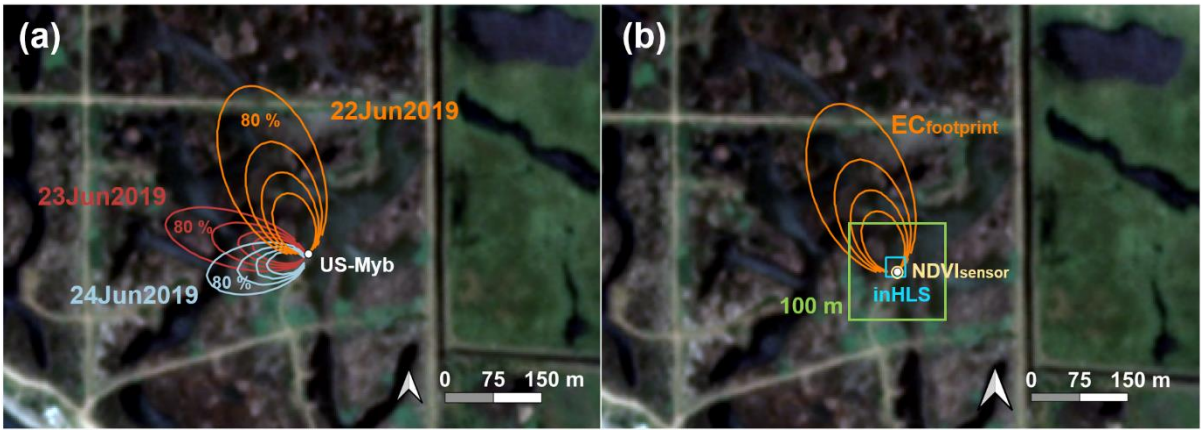

Figure 3 Examples of footprints for the US-Myb (Palustrine wetland) flux tower (white dot) between 1030hh to 1230hh (a) Daily eddy covariance (EC) footprints from June 22, 2019, to June 24, 2019. (b) eddy covariance footprint on June 22, 2018 (orange), a fixed 100 m × 100 m footprint (green) around the eddy covariance tower, and Harmonized Landsat/Sentinel (inHLS) pixels (cyan) including the normalized difference vegetation index (NDVI) sensor footprint (yellow) (Table 2). Contour lines denote footprints within which 50 – 80% (10% interval) of the cumulative flux originated. Image source: Planet Fusion RGB surface reflectance product for June 22, 2019 (projection, WGS84/UTM zone 10N). Footprints for *in situ* measurements at other sites are shown in (Figure A3 and A4).

Table 2 Footprint types used in this study (Figure 3) and Abbreviations used to indicate data source, footprint type (i.e., $NDVI_{sensor}$, inHLS, 100m, $EC_{footprint}$) (Figure 2), and temporal scale (i.e., satellite overpassing time and daily) for NIRv, NIRvP, and PAR in this study. PF refers to Planet Fusion (Section 2.3); MODIS refers to nadir bidirectional reflectance distribution function adjusted reflectance product using MODIS data; HLS refers to Harmonized Landsat and Sentinel (Section 2.3), BESS refers to the satellite-based Breathing Earth System Simulator which is a platform to compute fluxes in carbon, water, and energy.

Footprint type	**Description**
$NDVI_{sensor}$	Footprint of the normalized difference vegetation index (NDVI) sensor. Diameter: 12 – 20 m
inHLS	Harmonized Landsat/Sentinel (HLS) pixel coverage that includes $NDVI_{sensor}$ Pixel size: 30 m × 30 m
100 m	A fixed 100 m × 100 m area centered on the flux tower
$EC_{footprint}$	Daily eddy covariance (EC) measurement footprint
Relevant aspect	**Abbreviation examples**

Temporal scale	NIRv (satellite overpassing time), daily NIRv (daily time scale)
Data source	$\mathrm{NIRv}^{in\ situ}$, $\mathrm{NIRv}^{\mathrm{PF}}$, $\mathrm{NIRv}^{\mathrm{MODIS}}$, $\mathrm{NIRv}^{\mathrm{HLS}}$, $\mathrm{PAR}^{\mathrm{BESS}}$, $\mathrm{PAR}^{in\ situ}$
Footprint type	$\mathrm{NIRv}_{\mathrm{NDVIsensor}}$, $\mathrm{NIRv}_{\mathrm{inHLS}}$, $\mathrm{NIRv}_{\mathrm{100m}}$, $\mathrm{NIRv}_{\mathrm{ECfootprint}}$
All combined	$\mathrm{NIRv}^{\mathrm{PF}}_{\mathrm{ECfootprint}}$, $\mathrm{NIRv}^{\mathrm{PF}}_{\mathrm{100m}}$, daily $\mathrm{NIRvP}^{\mathrm{PF}}_{\mathrm{ECfootprint}}$, daily $\mathrm{PAR}^{\mathrm{BESS}}$

To evaluate the time series of NIRvP data against tower GPP data, we used nonparametric singular spectrum analysis, which decomposes and reconstructs time-series data to detect trends, remove long-term trends, and emphasize short-term variation (Ghil et al., 2002; Mahecha et al., 2007). A time series can be regarded as a collection of additive components (e.g., trends, regular oscillations, and noise (Ghil et al., 2002)); therefore, we evaluated both trends (with low-frequency, smooth components) and oscillations (with high-frequency coherence). Singular spectrum analysis in this study consisted of two stages: decomposition and reconstruction. During the decomposition stage, we formed a time window with length L, which is half of the study period (L = N/2, where N is the length of a flux measurement with a unit of days), for each site and slid it along the time series to construct the L × K (K = N–L + 1) Hankel matrix **X**. Then, we applied singular value decomposition to **X** to extract the eigenvalues and eigenvectors of $\mathbf{XX}^{\mathrm{T}}$. The leading singular value decomposition component (indicated by the largest eigenvalue) typically corresponds to the time-series trend (Alexandrov, 2009); therefore, we reconstructed the trend by inverting the projection from the leading component to a time series with length N. Subsequently, high-frequency (detrended) components were computed as the difference between the original time series and the trend. We conducted singular spectrum analysis using the R package *Rssa* v1.0.2 (Golyandina et al., 2018).

3. Results

This section reports the performance of Planet Fusion derived NIRv and NIRvP across different footprint types against *in situ* NIRv, NIRvP, and GPP.

3.1 Comparison of Planet Fusion NIRv and NIRvP with *in situ* NIRv and NIRvP

Planet Fusion NIRv in the footprint of *in situ* NDVI sensor ($\mathrm{NIRv}^{\mathrm{PF}}_{\mathrm{NDVIsensor}}$) showed better agreement with *in situ* NIRv ($\mathrm{NIRv}^{in\ situ}$) ($R^2 = 0.74$) compared to MODIS-derived NIRv ($\mathrm{NIRv}^{\mathrm{MODIS}}$) ($R^2 = 0.44$) or HLS-derived NIRv ($\mathrm{NIRv}^{\mathrm{HLS}}$) ($R^2 = 0.69$) (Figure 4). Even for daily gap-filled Planet Fusion data, linear relationships with $\mathrm{NIRv}^{in\ situ}$ were strong ($R^2 > 0.82$), with small RMSE values (< 0.1) at sites US-Bi2 (Corn), US-Snf (Pasture), US-Tw4 (Freshwater wetland), and US-Myb (Palustrine wetland) (Table A5). At US-Bi1 (Alfalfa), the relationship between $\mathrm{NIRv}^{\mathrm{PF}}_{\mathrm{NDVIsensor}}$ and $\mathrm{NIRv}^{in\ situ}$ had the highest RMSE (0.12). At all sites except US-Bi1(Alfalfa), the performance of $\mathrm{NIRv}^{\mathrm{PF}}_{\mathrm{NDVIsensor}}$

derived from gap-filled process in comparison with $NIRv^{in\ situ}$ was similar to the performance of $NIRv^{PF}_{NDVIsensor}$ derived from direct observation (Figure 5; Table A5). For NIRvP, regression analysis of $NIRvP^{PF}_{NDVIsensor}$ and $NIRvP^{in\ situ}$ at all sites showed strong linear relationships (R^2 = 0.83) with positive bias. Regression analysis of $NIRvP^{MODIS}$and $NIRvP^{in\ situ}$ showed strong linear relationships at all sites, but with varying slopes (Figure 5). Thus, the overall performance of $NIRvP^{MODIS}$ in comparison with $NIRvP^{in\ situ}$ (R^2 = 0.51) was worse than the overall performance of $NIRvP^{PF}_{NDVIsensor}$ (R^2 = 0.79) and $NIRvP^{HLS}$ (R^2 = 0.73) against $NIRvP^{in\ situ}$, which had more consistent slopes (Figure 5, Table A5). Unlike the impacts of gap-filling on NIRv, gap-filled $NIRvP^{PF}_{NDVIsensor}$ showed a stronger linear relationship with $NIRvP^{in\ situ}$ (R^2 = 0.90 – 0.98) than did $NIRvP^{HLS}$ (R^2 = 0.64 – 0.96). Meanwhile, gap-filled $NIRvP^{PF}_{NDVIsensor}$ showed a stronger linear relationship with $NIRvP^{in\ situ}$measurements at all sites (R^2 = 0.90 – 0.98) compared to observed $NIRvP^{PF}_{NDVIsensor}$ (R^2 = 0.88 – 0.98) (Figure 5; Table A5). In each site and all sites pooled data, the proportion of observed Planet Fusion out of gap-filled Planet Fusion was 49 – 56% when the proportion of HLS out of that was 22 – 28% (Figure 4; Table A5).

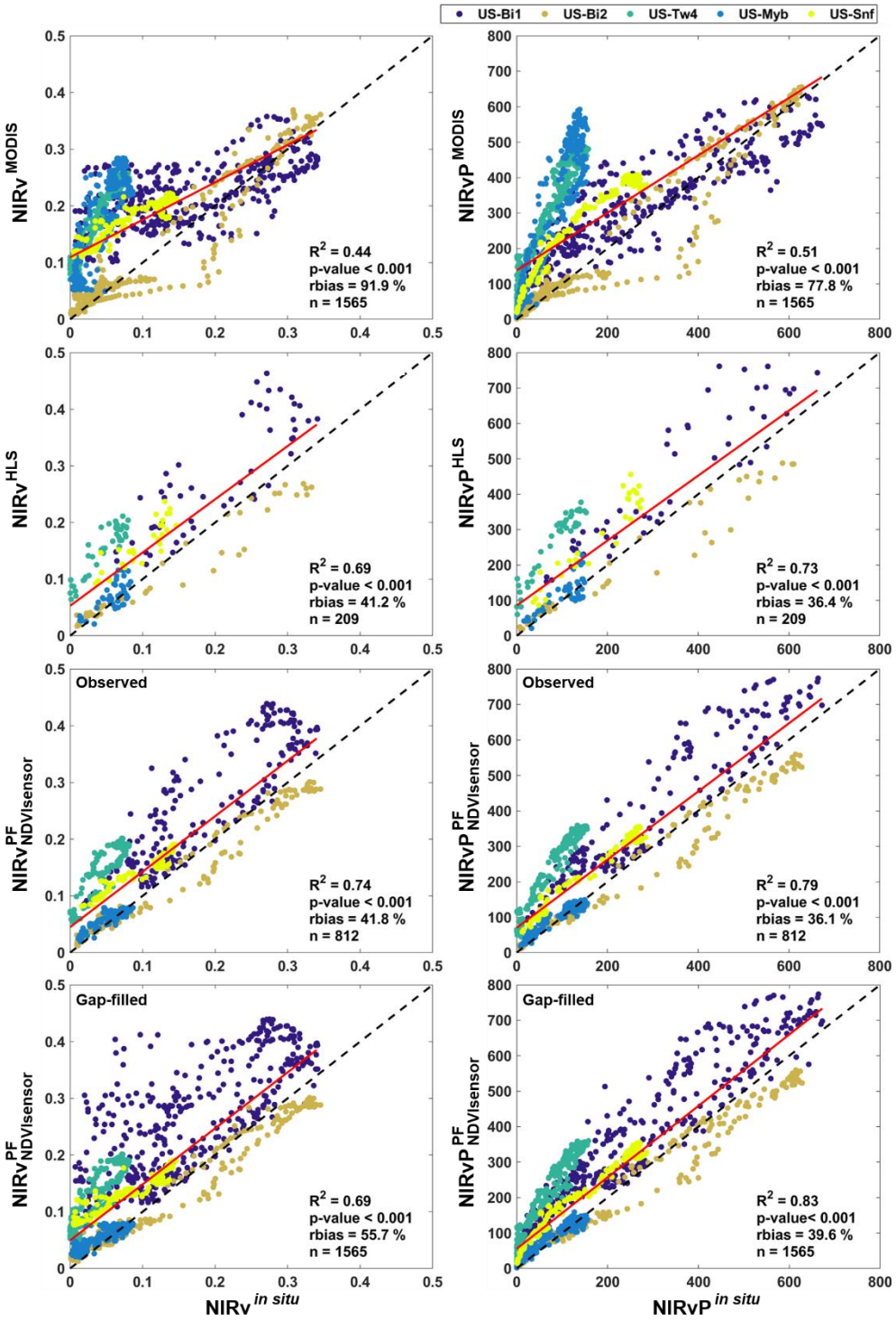

Figure 4 Comparison of measured *in situ* near-infrared radiation reflected from vegetation (NIRv) and the product of NIRv and photosynthetically active radiation (PAR) (NIRvP) around the satellite passing time with MODIS, HLS, observation-derived and gap-filled Planet Fusion (PF) data. Dashed black lines are 1:1 line (y = x). Red lines indicate linear regression model slopes for all sites. R^2 is the coefficient of determination, p-value indicates the significance of the linear regression, rbias is relative bias, and n is the number of samples used in the linear regression model. NIRv is unitless and NIRvP is in unit of μmol m^{-2} s^{-1}. Detailed analyses for each site are shown in (Table A5).

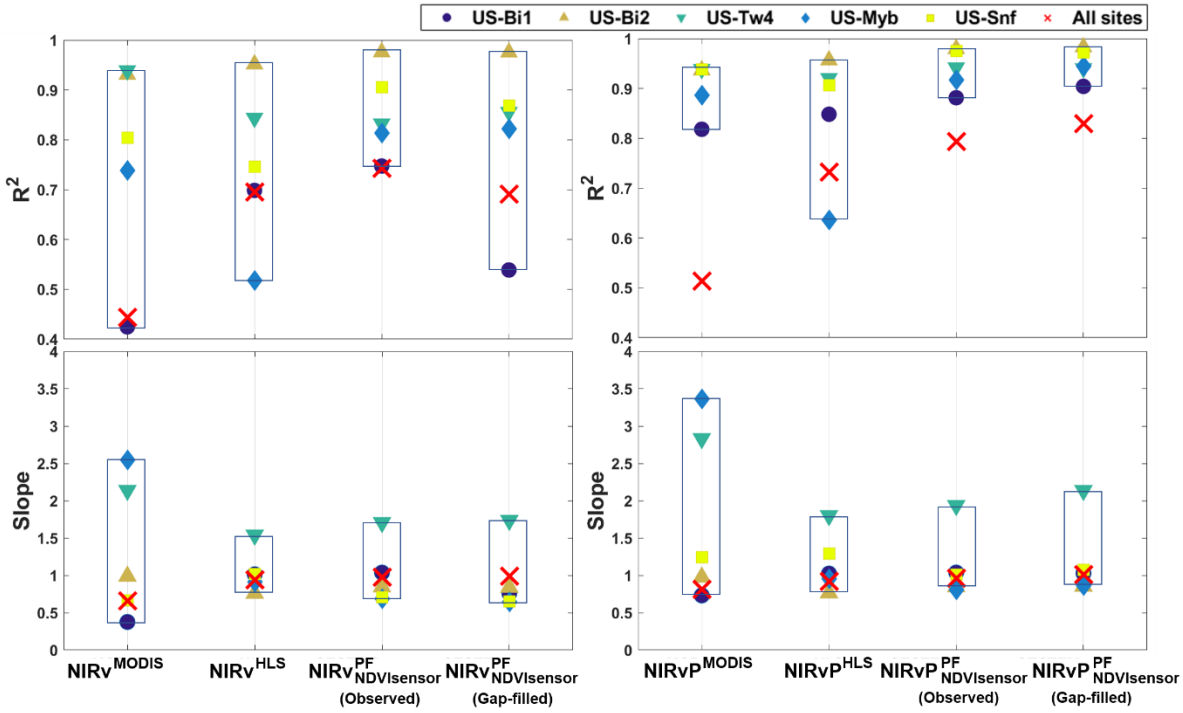

Figure 5 Comparison of measured *in situ* NIRv and NIRvP around the satellite passing time at each site and all sites pooled (colored symbols) with MODIS, HLS, and observation-derived and gap-filled Planet Fusion (PF) data. R^2 and the linear regression slope are indicated for each site. Detailed site data are provided in (Table A5).

3.2 Comparison of instantaneous Planet Fusion NIRv and NIRvP with against tower GPP estimates

$NIRvP^{PF}$ ($R^2 \leq 0.78$) performed better than $NIRvP^{in\ situ}$ ($R^2 = 0.61$) in estimating GPP when combining the data from all sites (Figure 6). The linear relationships between NIRvP and GPP for all site data combined showed the following ranking (in order of decreasing R^2): Planet Fusion NIRvP in daily flux tower footprints ($NIRvP^{PF}_{ECfootprint}$) > Planet Fusion NIRvP in a a fixed area footprint area around flux tower (100 m × 100 m) ($NIRvP^{PF}_{100m}$) > Planet Fusion NIRvP in the footprint of *in situ* NDVI sensor ($NIRvP^{PF}_{NDVIsensor}$) > *in situ* NIRvP ($NIRvP^{in\ situ}$), with R^2 values of 0.78, 0.65, 0.61, and 0.61, respectively. On the other hand, the linear relationships between NIRv and GPP were moderate (in order of decreasing R^2): $NIRv^{PF}_{ECfootprint}$ > $NIRv^{in\ situ}$ > $NIRv^{PF}_{100m}$ > $NIRv^{PF}_{NDVIsensor}$, with R^2 values of 0.62, 0.58, 0.46, and 0.43, respectively. Overall, the linear relationships were stronger between $NIRvP^{PF}$ and GPP than between $NIRv^{PF}$ and GPP (Figures 6, 7).

The performance of $NIRvP^{PF}$ in estimating GPP at each site individually was only clearly improved for one (US-Myb, Palustrine wetland) out of the five sites when the satellite footprint was matched to the $EC_{footprint}$ (Figure 7, Table A6). For other sites the performance of the $NIRvP^{PF}_{ECfootprint}$ was slightly better (US-Bi1, Alfalfa; and US-Snf, Pasture) or comparable (US-Bi2, Corn; and US-Tw4, Freshwater wetland) than other footprint types. $NIRvP^{PF}_{ECfootprint}$ showed a strong linear relationship with *in situ*

GPP at the wetland sites, especially US-Myb (Palustrine wetland). For all footprint types, $NIRvP^{PF}$ generally showed slightly stronger linear relationships with GPP than with $NIRvP^{in\ situ}$ except for US-Bi2 (Corn). We observed the largest improvement of $NIRvP^{PF}$ compared to $NIRvP^{in\ situ}$ for site US-Bi1 (Alfalfa), where the linear regression between $NIRvP^{in\ situ}$ and GPP had an R^2 value of 0.72, whereas the linear regression of $NIRvP^{PF}$was > 0.78 for all footprint types (Table A6). $NIRv^{PF}_{ECfootprint}$ also had higher R^2 values compared to $NIRv^{PF}_{100m}$ (Figure 7; Table A6).

The slopes of linear regressions between $NIRv^{PF}$ and $NIRvP^{PF}$ and GPP showed large differences for the $NDVI_{sensor}$ and 100 m footprints but converged when Planet Fusion data was matched with the footprint type of $EC_{footprint}$ (Figure 6). More specifically, the variability in linear regression slopes of both NIRv and NIRvP with GPP showed the following ranking (in order of decreasing variability): Planet Fusion NIRv (NIRvP) with different footprint types ($EC_{footprint}$ > 100m > $NDVI_{sensor}$) > $NIRv^{in\ situ}$($NIRvP^{in\ situ}$) (Figure 7). In the cropland sites, the linear regression slopes of $NIRv^{in\ situ}$ and $NIRvP^{in\ situ}$ with GPP were larger at US-Bi2 (Corn, a C4 plant) than at US-Bi1 (Alfalfa, a C3 plant). These trends were also observed in both $NIRv^{PF}$ and $NIRvP^{PF}$ for all footprint types (Figure 6; Table A6). The linear regression slopes of $NIRv^{in\ situ}$ and $NIRvP^{in\ situ}$ with GPP were generally larger in wetland sites than in cropland sites.

While overall NIRvP showed better GPP estimation performance than NIRv, there were notable differences between Planet Fusion and *in situ* – based results as well as individual sites vs. pooled data (Figures 6, 7, S3; Table A6). For the pooled data from all sites, the difference in R^2 values between NIRvP and NIRv-based GPP estimation showed a ranking in the following order: Planet Fusion NIRv (NIRvP) with different footprint types($NDVI_{sensor}$-> 100m > $EC_{footprint}$) > $NIRv^{in\ situ}$($NIRvP^{in\ situ}$) with R^2 differences of 0.18, 0.19, 0.16, and 0.02, respectively (Table A6). For individual sites, *in situ* only showed clear improvement of NIRvP over NIRv for US-Myb (Palustrine wetland), while for other sites the performances were comparable (US-Snf; Pasture) or even slightly worse (US-Bi1, Alfalfa; US-Bi2, Corn; US-Tw4, Freshwater wetland) for NIRvP (Table A6). For Planet Fusion-based results, larger improvements of NIRvP over NIRv were observed, especially for sites US-Bi1(Alfalfa) and US-Myb (Palustrine wetland) (Figure 7). However, for some sites, and especially for the 100 m fixed footprint type, NIRvP performed slightly worse than NIRv.

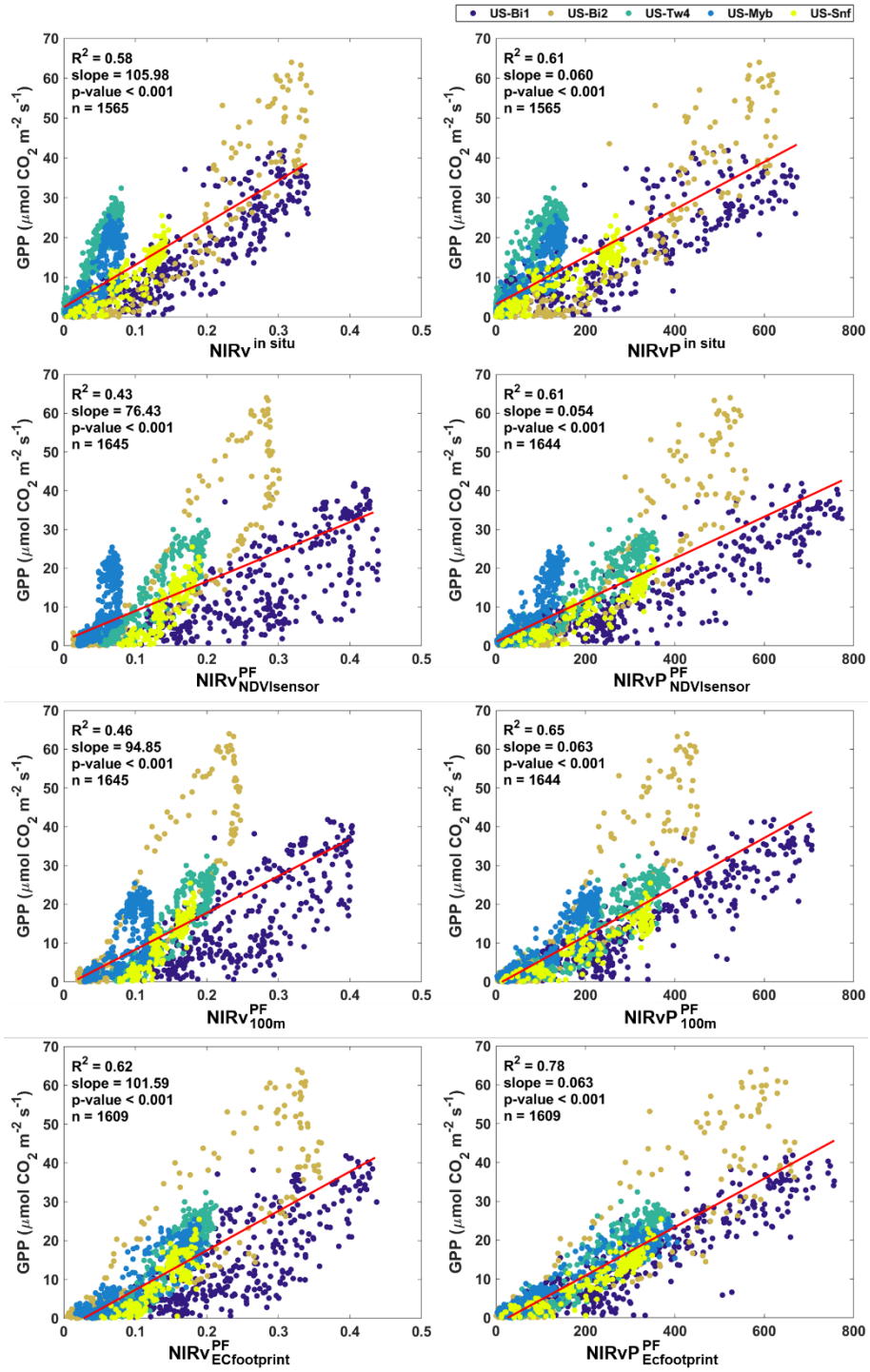

Figure 6 Comparison of NIRv and NIRvP measured *in situ* and derived from gap-filled Planet Fusion (PF) in different footprint types with GPP measured in all study sites (colored circles) around satellite overpassing time. NIRv(NIRvP)$^{PF}_{NDVIsensor}$, NIRv(NIRvP)$^{PF}_{100m}$, NIRv(NIRvP)$^{PF}_{ECfootprint}$ denotes Planet Fusion -derived NIRv (NIRvP) around the local satellite overpassing time for footprint domains (i.e., $NDVI_{sensor}$, 100m, and $EC_{footprint}$). Red lines indicate linear regression model slopes for all sites. R^2 is the coefficient of determination, p-value indicates the significance of the linear regression, and n is the number of samples used in the linear regression model. NIRv is unitless and NIRvP is unit of μmol m^{-2} s^{-1}. Detailed site data are provided in (Table A6).

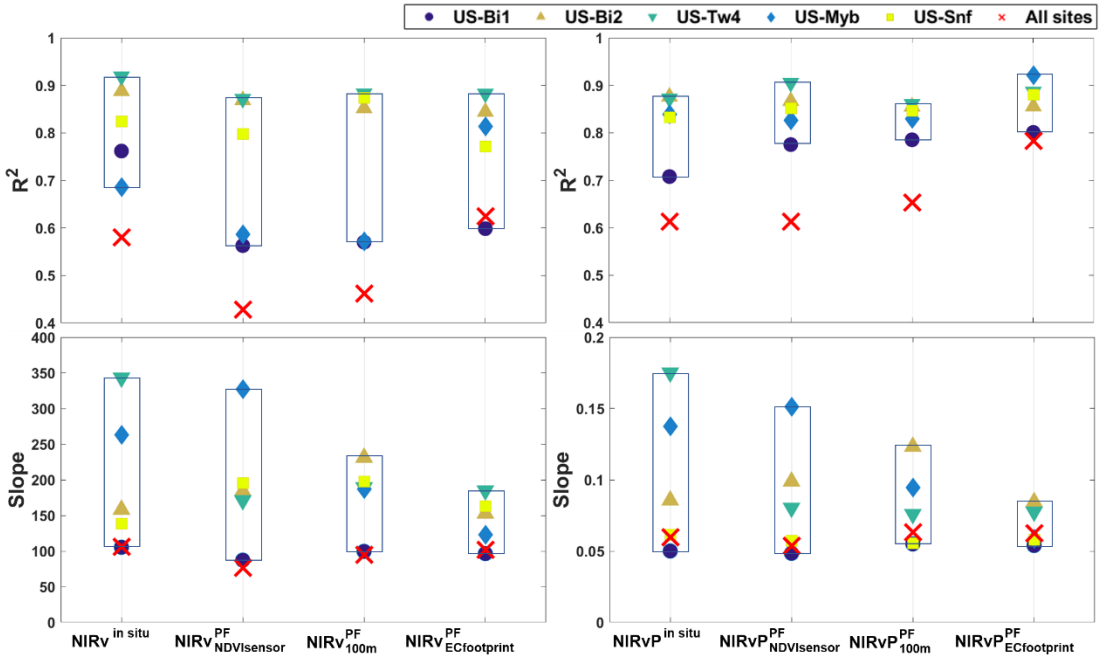

Figure 7 Comparison of NIRv and NIRvP measured *in situ* and derived from gap-filled Planet Fusion (PF) with GPP measured at each site and all sites pooled (colored symbols) around satellite passing time for all footprint types. $NIRv(NIRvP)^{PF}_{NDVIsensor}$, $NIRv(NIRvP)^{PF}_{100m}$, $NIRv(NIRvP)^{PF}_{ECfootprint,satellite}$ denotes Planet Fusion-derived NIRv (NIRvP) around the local satellite overpassing time for footprint domains (i.e., $NDVI_{sensor}$, 100m, and $EC_{footprint}$). R^2 and linear regression slopes are shown for each site. Detailed site data are provided in (Table A6).

Trends in $NIRvP^{PF}_{ECfootprint}$ and GPP over time were similar (Figure 8). Among Planet Fusion NIRvP data derived from different footprint types, $NIRvP^{PF}_{ECfootprint}$ showed generally good performance in tracking the detrended GPP, especially over wetlands. For example, at site US-Myb (Palustrine wetland), $NIRvP^{PF}_{ECfootprint}$ captured the sharp drops in GPP around day of the year 160, 260 and 280, whereas $NIRvP^{PF}_{NDVIsensor}$ and $NIRvP^{PF}_{100m}$ did not (Figure S3). $NIRvP^{PF}_{ECfootprint}$ showed stronger linear relationships with GPP, compared with $NIRvP^{in\ situ}$. Notably, the R^2 values of the relationship between detrended $NIRvP^{PF}_{ECfootprint}$ and detrended GPP were greater than the R^2 values for $NIRvP^{in\ situ}$, except for US-Bi2 (Corn).

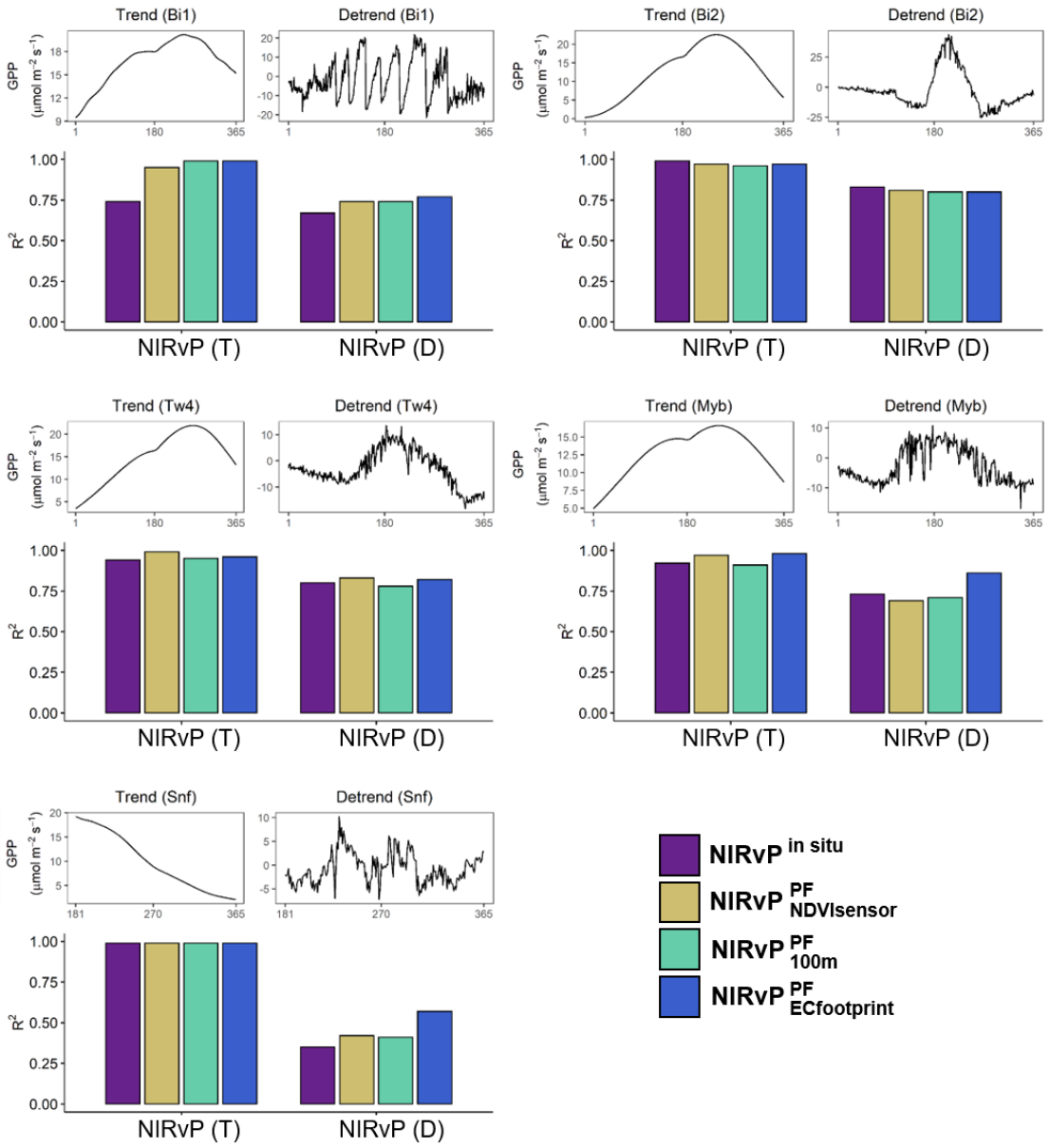

Figure 8 The GPP trend (T) and detrended (D) GPP at each site. Linear relationships of gap-filled Planet Fusion (PF) NIRvP and *in situ* NIRvP with T and D around the satellite passing time are also shown. $NIRvP^{PF}_{NDVIsensor}$, $NIRvP^{PF}_{100m}$, $NIRvP^{PF}_{ECfootprint}$ denotes Planet Fusion -derived NIRvP around the local satellite overpassing time in different footprint type (i.e., $NDVI_{sensor}$, 100m, and $EC_{footprint}$). Detailed site data for the entire study period are shown in (Figure S3).

$NIRvP^{PF}_{ECfoorprint}$ more accurately estimated GPP around satellite overpassing time at the original spatial resolution (3 m), compared with footprint matching at the aggregated 30 m resolution (Figure 9). The performances of $NIRvP^{PF}_{ECfootprint}$ in estimating GPP at different spatial resolutions were similar for croplands but differed for wetland sites. For example, in the wetland sites (i.e., US-Tw4, Freshwater wetland; US-Myb, Palustrine wetland; and US-Snf, Pasture), $NIRvP^{PF}_{ECfootprint}$ (3 m) showed a slightly stronger linear relationship (R^2 = 0.89, 0.92, and 0.88, respectively) with GPP than did 30 m resampled $NIRvP^{PF}_{ECfootprint}$(R^2 = 0.83, 0.90, and 0.85, respectively).

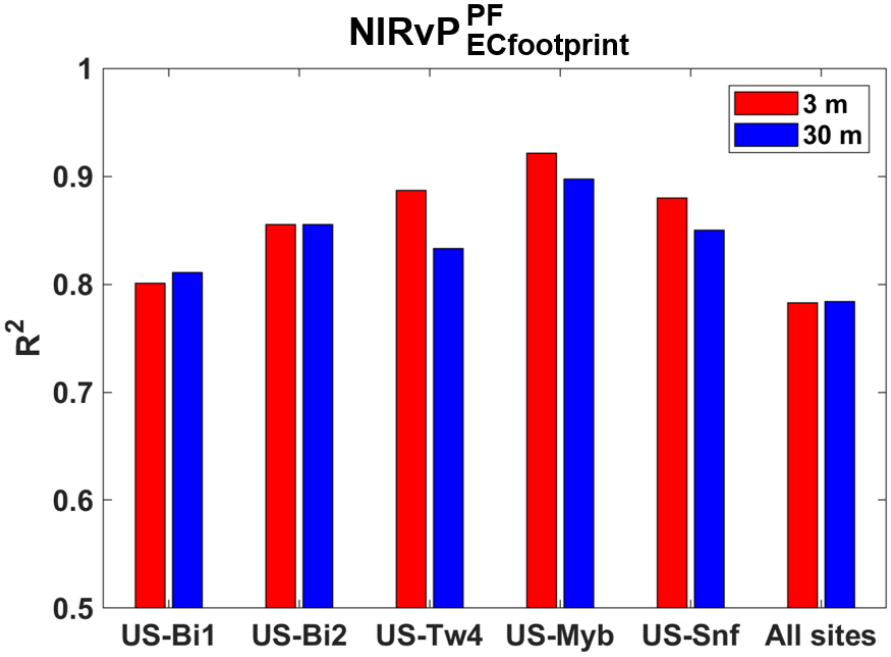

Figure 9 Evaluation of Planet Fusion (PF) derived NIRvP within eddy covariance (EC) footprint in different spatial resolution against GPP around satellite passing time. $NIRvP^{PF}_{ECfootprint}$ denotes Planet Fusion -derived NIRvP in daily eddy covariance footprints around the local satellite overpassing time. The linear relationships against GPP are shown. The detailed numbers are in (Table A6).

3.3 Daily GPP estimation from Planet Fusion -derived NIRvP

The overall performance of daily $NIRvP^{PF}_{ECfootprint}$ (R^2 = 0.80; RMSE = 2.08) in estimating daily GPP was considerably better than the overall performance of daily $NIRvP^{in\ situ}$ (R^2 = 0.67; RMSE = 2.68) (Figure 10). The $NIRv^{PF}_{ECfootprint}$× daily PAR^{BESS} product showed a stronger linear relationship and smaller RMSE (R^2 = 0.79; RMSE = 2.15) with daily GPP than the $NIRv^{in\ situ}$ × daily PAR^{BESS} product (R^2 = 0.62; RMSE = 2.88). Compared with daily $NIRvP^{PF}_{ECfootprint}$, $NIRv^{PF}_{ECfootprint}$ × daily PAR^{BESS} showed similarly good performance for daily GPP estimation. The slopes (in parentheses) estimated by linear regression between NIRvP and daily GPP were: daily $NIRvP^{PF}_{ECfootprint}$ (0.67–0.98) > $NIRv^{PF}_{ECfootprint}$ × daily PAR^{BESS} (0.69 – 1.01) > daily $NIRvP^{in\ situ}$ (0.80 – 2.32) > $NIRv^{in\ situ}$ × daily PAR^{BESS} (0.68 – 2.35) (Table A7). Additionally, $NIRv^{PF}_{ECfootprint}$ × daily PAR^{BESS} followed well the changes of GPP with time (Figure 11).

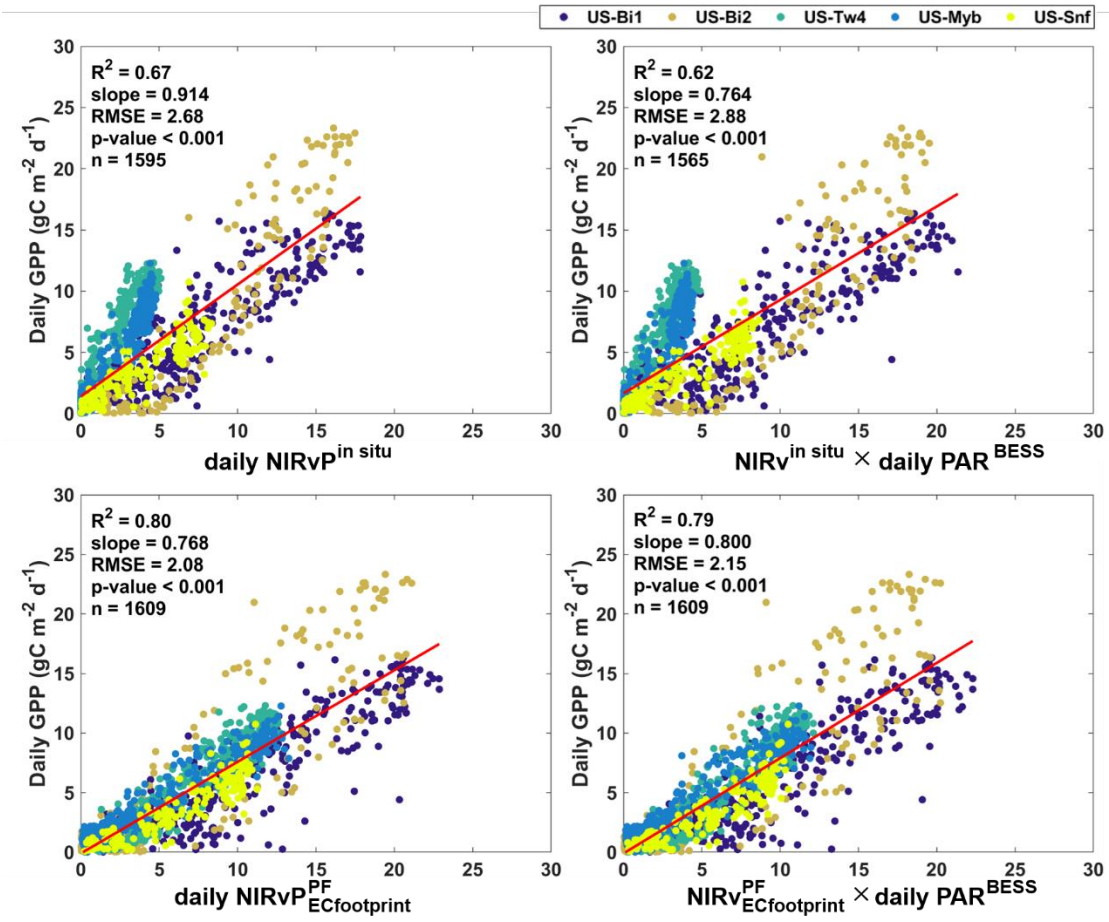

Figure 10 Linear relationships between *in situ*-measured and Planet Fusion (PF)-derived daily NIRvP and daily GPP at all sites (colored circles). daily $NIRvP^{in\ situ}$ denotes the aggregated half-hourly *in situ* NIRvP; $NIRvP^{in\ situ}$ denotes averaged *in situ* NIRvP around the local satellite overpassing time; daily PAR^{BESS} means daily summed PAR data retrieved from the satellite-based Breathing Earth System Simulator (BESS); daily $NIRvP^{PF}_{ECfootprint}$ indicates temporally upscaled $NIRv^{PF}_{ECfootprint}$. Red line indicates the linear regression model slope of overall sites. R^2 is the coefficient of determination, p-value indicates the significance of the linear regression, and n is the number of samples used in the linear regression model. NIRvP is given in unit of mol m^{-2} d^{-1}. Detailed site data are provided in (Table A7).

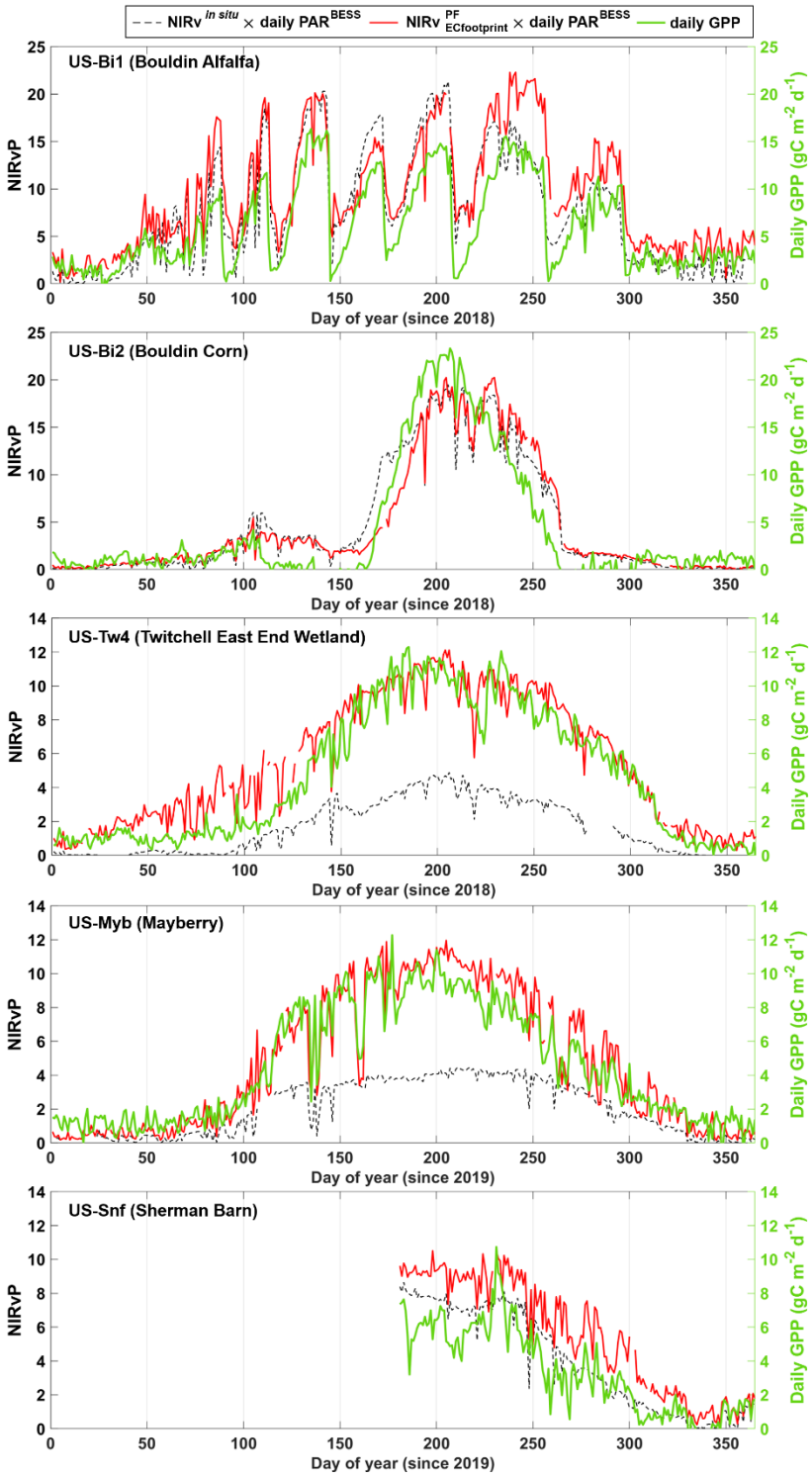

Figure 11 Seasonal variation of the product of NIRv from *in situ* and Planet Fusion (PF) in different footprint types and BESS daily PAR (left axis) and that of daily GPP (right axis). NIRvP is given in unit of mol m^{-2} d^{-1}.

4. Discussion

Overall, we found that matching Planet Fusion NIRvP to the flux tower footprint considerably

improved the agreement with flux tower-based GPP across sites compared to using a fixed footprint (100 m, a hectare area around tower; $NDVI_{sensor}$, the footprint of *in situ* NDVI sensor) even when compared to the *in situ* NIRvP observations (Figure 6 and 7). The effects of matching the flux tower footprint on the regression slope between NIRvP and GPP was largest for the two wetland sites and a corn site (Figure 7). For daily GPP estimation from Planet Fusion data, the different approaches showed comparable performances (Figure 10). NIRvP considerably outperformed NIRv for GPP estimation around satellite overpass time, especially when pooling the data from all sites and using Planet Fusion NIRvP. A more detailed discussion on the different aspects is presented in the subsections below.

4.1 Flux tower footprint matching and effects of spatial and temporal resolution on GPP estimation

The high spatial resolution of Planet Fusion NIRvP ($NIRvP^{PF}$) (3 m) allowed us to match the footprints of *in situ* NDVI sensors and eddy covariance systems with Planet Fusion pixels, which led to considerable improvement in the agreement between $NIRvP^{PF}$ and flux tower GPP compared to either a fixed footprint (100 m by 100m) or the relatively small area covered by *in situ* NDVI sensors (NDVIsensor footprint)(Figure 3, 6, and 7). In fact, the performance of Planet Fusion NIRvP in daily flux tower footprints ($NIRvP^{PF}_{ECfootprint}$) was even better than that of *in situ* sensors with bi-hemispheric view, which did not fully cover the EC footprint (Figure 3). This is a remarkable finding as it implies that the uncertainties associated with satellite observations of NIRvP are smaller than the impacts of the footprint mismatch between *in situ* optical sensors and the flux tower footprint.

An important aspect of our study was to characterize how the footprint mismatch affected the NIRvP-GPP relationships and to identify the factors explaining such patterns. We found that the effects of footprint mismatch had relatively small impacts on the NIRvP-GPP correlation for individual sites but large impacts on the data combined from all sites (Figure 6 and 7). This was due to inconsistent NIRvP-GPP regression slopes when the flux tower footprint was not matched (Figure 7). These results indicate that while the temporal GPP dynamics are relatively consistent in different parts of the ecosystems, the canopy structure factors such as leaf area index, leaf angles and clumping to which NIRvP is sensitive (Dechant et al., 2022; Dechant et al., 2020) can vary considerably within the flux tower footprints. Freshwater wetland (US-Tw4) and Palustrine wetland (US-Myb) showed the highest sensitivity of regression slopes to the choice of footprint schemes (Figure 6 and 10). Although one might first suspect the impact of the water fraction or the spatial patterns of the water (Matthes et al., 2014) rather than vegetation canopy structure in the footprint of optical sensors to explain the different slopes in wetland ecosystems, NIRvP is largely insensitive to water background as both the NDVI factor and NIR reflectance have low values for water (Chen et al., 2018; Weiss and Crabtree, 2011). Therefore, the most likely explanation for the large sensitivity of wetland sites to the footprint type is the spatial heterogeneity in canopy structure. Apart from insufficient spatial coverage (Gamon, 2015), observations

from *in situ* spectral sensors can also be particularly biased as they typically include the tower structure and its surroundings which are not representative of the flux tower footprint as vegetation near the tower is cleared for the safety of the tower structure. The high consistency between NIRvP and GPP patterns at each site during the study period (Figure 11 and S3) is likely due to the strong impact of environmental drivers such as PAR, temperature and humidity.

We found that the NIRvP-GPP relationships indeed improved by footprint matching rather than other factors that could affect the relationship. As NIRvP is only a proxy for GPP but not a direct observation, the comparison of satellite NIRvP with ground GPP is not a direct ground validation and might be affected by other limitations of NIRvP to estimate GPP, in addition to other uncertainties related to satellite vs. ground observations. Therefore, we used two different ways to exclude such uncertainties as alternative factors explaining our findings of improved NIRvP-GPP relationships when matching Planet Fusion with flux tower footprints. First, we compared entirely *in situ*-based NIRvP-GPP relationships with relationships where the Planet Fusion area matched the footprint of the *in situ* NDVI sensor. As these results showed rather similar patterns in slope differences between sites (Figure 6 and 7), the main factor for different slopes indeed seems to be the footprint size and site location. Second, we also conducted a direct ground-validation analysis for NIRv and NIRvP and found strong agreement between Planet Fusion and *in situ* NIRv and NIRvP (Figure 4 and 5). This further confirms that the Planet Fusion -based satellite products are reliable and that the patterns in the results of NIRvP-GPP relationships for different footprints are indeed due to the area covered rather than other sources of uncertainty. Although we found the footprint mismatch to be the dominant factor explaining NIRvP-GPP slope differences between sites, the photosynthetic pathway of the vegetation also needs to be taken into account. Among the cropland sites, the slope of Planet Fusion NIRvP against GPP in C4 plants (corn in US-Bi2) was generally higher than that in C3 plants (alfalfa in US-Bi1) (Figure 6). This higher slopes of C4 compared to C3 plants is consistent with previous studies although we found a smaller difference (Badgley et al., 2019; Baldocchi et al., 2020; Dechant et al., 2022). We found that the gap-filling of Planet Fusion data had the effect of increasing the spread in NIRvP-GPP regression slopes (Figure 5). This effect, however, was small and mostly due to a single site (US-Myb; Palustrine wetland) and also cannot explain the differences between different footprint types as the gap-filled data was used for all of them.

The high spatial resolution of Planet Fusion improved the performance of NIRvP-based GPP estimation more compared to the high temporal resolution. To quantify the effects of spatial and temporal resolution of satellite imagery on the NIRvP-based GPP estimation results, we conducted further analyses. First, we evaluated if the footprint matching could still be effective at the coarser spatial resolution of 30 m instead of 3 m. Although the performance of 30 m data was still relatively robust, better performance (R^2 increase ~ 0.06) was found for 3 m at some of the sites, especially at the wetland and corn sites (Figure 9; Table A6), where the water surface extent can change at scales below

30 m (Halabisky et al., 2016). In the direct ground validation for NIRv and NIRvP, we found that the coarse 500 m MODIS pixels had poor performance with large slope differences between the sites (Figure 4 and 5) due to low proportion of footprint area within a pixel (McCombs et al., 2019), while the finer 30 m HLS and 3 m Planet Fusion pixels showed robust performance. Nevertheless, we found substantial land surface heterogeneity even within the 30 m satellite pixels (Figure A8) indicating the advantage of the Planet Fusion high-resolution imagery which cannot be replaced by fusion products based on MODIS-HLS without compromising the performance (Kong et al., 2021). Second, we evaluated the impact of temporal resolution by comparing the results for daily matching of the EC footprint with that of matching the annual footprint (Figure A9). We found similar performance in the two cases. Although there is daily variation in the footprints at each site, the annual footprints are good representatives of the area measured by the flux tower because of a strongly dominant wind direction related to the typical meteorological conditions in this area on an annual time scale (Figure A3; Figure S8). These findings are, therefore, specific to the sites we used and bigger differences between annual and daily footprint matching are expected for other sites with more variable wind directions (Kim et al., 2006).

The near-daily revisit frequency of CubeSats (Roy et al., 2021) allowed us to track canopy dynamics in detail. For the study period in each site, overall, CubeSats provided 49 – 56% of daily data when gap-filled data is removed, which is a higher daily retrieval rate compared to HLS (22 – 28%) (Figure 4; Table A5). The near-daily Planet Fusion acquisition frequency enabled the detection of surface changes like mowing events (Figure S3 and S4) (Kong et al., 2021). Nonetheless, cloud-induced data gaps can still present a significant obstacle for uninterrupted land surface monitoring. Over the study sites, the Planet Fusion -based gap-filling process enabled daily tracking of photosynthesis (Figure 5; Table A5). Even though the data-gaps were not negligible throughout the study period (Figure A8), Planet Fusion data were in general successfully gap-filled (Figure 4) in part due to relatively short temporal gaps (Kong et al., 2021; Luo et al., 2018). While the gap-filling had considerable impacts on NIRv, the performance of Planet Fusion NIRvP compared to *in situ* NIRvP was robust even for gap-filled data (Figure 4 and 5). Daily gap-filled $\mathrm{NIRvP}^{\mathrm{PF}}_{\mathrm{ECfootprint}}$ responded to GPP drops caused by drastic surface changes (e.g., mowing) (Figure 8; Figure S3) which agrees with previous findings that Planet Fusion -based evapotranspiration maps are able to capture evaporation fluxes on a day-to-day basis (Aragon et al., 2021). Further improvements in the capacity to track diurnal canopy dynamics may involve spatio-temporal image fusion between CubeSat and geostationary satellites that scan the same area in every 5-15 minutes (Khan et al., 2021) or integration of ECOSTRESS data that measure thermal infrared with 70 m resolution every 1-5 days (Fisher et al., 2020; Li et al., 2021).

4.2 Roles of radiation component in GPP mapping

At the time of satellite overpass, we found $NIRvP^{PF}$ estimated GPP better than $NIRv^{PF}$ when pooling data from all sites and also for most sites individually (Figure 6, 7 and 8). When NIRv was first proposed, it successfully explained the variation of GPP at the monthly time scale (Badgley et al., 2017). As the variations of daily NIRv and, above all, PAR values are mostly averaged out at monthly time scales, NIRv alone can estimate monthly GPP with reasonable performance. However, NIRv alone raises an issue for GPP estimation at the time of satellite overpass and daily scales as PAR plays an important role (Dechant et al., 2022; Dechant et al., 2020). Although PAR variations are most important for estimating diurnal variations of GPP and NIRvP, PAR still plays an important role at the time of satellite overpass due to considerable seasonal PAR variations (Figure A2 and S3). In fact, when examining our results closely, a stronger tendency towards non-linear relationships to GPP can be observed for NIRv compared to NIRvP when considering sites individually (Figure 7). Somewhat similar non-linear effects have also been reported before for statistical GPP estimation from reflectance measured by the hyperspectral sensor without including PAR information (Dechant et al., 2019). However, another potential explanation for the non-linear effects at rather low values could be the non-zero NIRv values for senescent or dead vegetation outside of the main growing season when GPP is essentially zero (Figure S3). As PAR is low during those times, NIRvP has a somewhat dampened non-linearity compared to NIRv. Assuming that background effects are indeed partly causing the non-linearities, using soil-adjusted NIRv may further improve the results (Jiang et al., 2021). Overall, the better performance of $NIRvP^{PF}_{ECfootprint}$ for estimating GPP (Figure 6; Table A6) is consistent with both a mechanistic understanding of GPP drivers and the previous literature on the matter.

While some aspects of the differences in performance of NIRv compared to NIRvP for GPP estimation (Figure 6 and 7) might appear counter-intuitive at first sight, a closer examination of the results can explain those patterns. In particular, the difference between NIRv and NIRvP for GPP estimation was considerably smaller for *in situ* data than for Planet Fusion data and for the latter it was considerably larger for pooled data from all sites than for individual sites. Furthermore, the slope consistency and R^2 values between sites showed similar relative sensitivities to footprints for $NIRv^{PF}$ and for $NIRvP^{PF}$ although the R^2 values differed considerably in absolute values. All these results can be understood by taking into account the effects of gap-filling on $NIRv^{PF}$, as the gap-filling led to decrease in agreement with *in situ* NIRv ($NIRv^{in\ situ}$) (Figure A8) but this larger disagreement essentially disappeared for NIRvP (Figure 4 and 5). This compensatory effect of PAR may also suggest a critical control of PAR on regulating seasonal GPP variations at the time of satellite overpass. It should be noted that the effect of gap-filling on the performance of $NIRv^{PF}$ was mostly reflected in the correlation to GPP at individual sites rather than in the slope consistency between sites (Figure 4 and 5).

Daily PAR maps enable $NIRv^{PF}$ maps to conduct spatial upscaling of daily GPP estimation from

point eddy covariance sites to landscape scale. Currently, estimates of GPP at eddy covariance sites cover only a small area of the terrestrial surface, with limited numbers of sites that are strongly biased geographically (Ciais et al., 2014; Schimel et al., 2015). We found that daily $\mathrm{NIRvP}^{\mathrm{PF}}_{\mathrm{ECfootprint}}$, which was temporally upscaled from satellite overpassing time, was strongly correlated to daily GPP (Figure 10) as GPP at a specific time of the day with a cosine correction generally shows a strong linear relationship with daily GPP (Ryu et al., 2012; Zhang et al., 2018). In other words, the relationship between $\mathrm{NIRvP}^{\mathrm{PF}}_{\mathrm{ECfootprint}}$ and GPP around the overpass time resulted in good performance of daily $\mathrm{NIRvP}^{\mathrm{PF}}_{\mathrm{ECfootprint}}$ in estimating daily GPP (Figure 10). Furthermore, NIRvP includes information regarding canopy structure and the amount of incoming radiation absorbed and scattered by vegetation (Baldocchi et al., 2020; Dechant et al., 2022; Dechant et al., 2020). Assuming that canopy structure changes are small within a day, the multiplication of daily PAR by Planet Fusion-derived NIRv will robustly estimate daily GPP. Consequently, $\mathrm{NIRv}^{\mathrm{PF}}_{\mathrm{ECfootprint}}$ × daily $\mathrm{PAR}^{\mathrm{BESS}}$ performed similarly to daily $\mathrm{NIRvP}^{\mathrm{PF}}_{\mathrm{ECfootprint}}$ in estimating daily GPP (Figure 10 and 11). Accordingly, Planet Fusion -derived NIRv combined with daily PAR maps enables us to generate daily GPP maps with a high degree of fidelity (Figure 10), which is consistent with the finding of previous studies at different scales (Jiang et al., 2021).

4.3 Limitations and perspectives

Our findings indicate that further tests of the slopes of the relationships between NIRvP and GPP are required. The study period for each site varied from 6 months to 1 year (Table 1), which may be sufficient for testing seasonal variation; however, it is insufficient for testing whether these slopes are stable over long periods. Several studies have reported strong correlations between NIRvP and GPP (Baldocchi et al., 2020; Dechant et al., 2022; Dechant et al., 2020), but the consistencies of their slopes over multiple years, which could include severe stress such as drought, have not been evaluated. Our study sites (cropland and wetlands) are well-known for low water stress. While Baldocchi et al. (2020) reported a strong and rather consistent relationship between NIRvP and GPP at an annual grassland site when pooling data from twelve years, the stability of slopes was not investigated. Also, the longer-term robustness of the relationships between NIRvP and GPP could differ between ecosystems. The accumulation of Planet Fusion data over longer periods will allow us to capture interannual variation in canopy GPP and test if the promising findings of Baldocchi et al. (2020) and Badgley et al. (2019) also hold at finer spatio-temporal scales across ecosystems.

Limitations are expected in the performance of NIRvP to capture shorter-term responses of GPP to vegetation stress as NIRvP is entirely based on canopy structure and radiation information and does not include physiological vegetation signals. In particular, NIRv closely approximates the product of the

fraction of absorbed PAR (fPAR) times the fraction of photons that escape from the canopy (fesc) (Zeng et al., 2019). Therefore, NIRvP well captures APAR, the product of fPAR and PAR, which is a strong driver of GPP. Although there is convincing evidence that fesc can capture seasonal variations in light use efficiency (LUE) in crops in the absence of strong environmental stress (Dechant et al., 2020; Liu et al., 2020), fesc might not capture the faster physiological responses at the onset of droughts as fesc is driven by canopy structure variables such as leaf area index, clumping and leaf inclination (Badgley et al., 2017; Qiao et al., 2019; Zeng et al., 2019), which typically respond more slowly than leaf physiology. Therefore, remote sensing variables that carry physiological signals related to LUE such as the photochemical reflectance index (PRI) and physiological emission yield of sun-induced chlorophyll fluorescence (Φ_F) should be considered to refine NIRvP-based estimates of GPP in situations of strong environmental stress (Dechant et al., 2022; Kimm et al., 2021; Wang et al., 2020). While SIF contains both the structural information of NIRvP and the physiological information of Φ_F, the variations of Φ_F tend to be so small that separating them from the structural component with the help of NIRvP might be necessary to use this information for improved GPP estimation (Dechant et al., 2022).

Uncertainties remain in the satellite products and *in situ* measurements. Because the radiometric accuracy of Planet Fusion data is linked to that of HLS (in this study) (Planet Fusion Team, 2021), the bias of HLS NIRv ($NIRv^{HLS}$) against $NIRv^{in\ situ}$ might lead to the bias of Planet Fusion NIRv in the footprint of *in situ* NDVI sensor ($NIRv^{PF}_{NDVIsensor}$) against $NIRv^{in\ situ}$ as (Figure 4). In addition, the absolute geolocation accuracy of the PlanetScope CubeSat data is less than 10 m RMSE (Planet Fusion Team, 2021). Therefore, the discrepancy between $NIRv^{PF}_{NDVIsensor}$ and $NIRv^{in\ situ}$ over US-Bi1 (Alfalfa), which was similar to the range of Planet Fusion NIRv in HLS pixel coverage that includes $NDVI_{sensor}$ ($NIRv^{PF}_{inHLS}$) (Figure A8), could be partly explained by geolocation uncertainties. Apart from the geolocation accuracy of the satellite imagery, the location of *in situ* spectral sensors can also contribute to biases in our results (Figure S1). Regarding the temporal patterns, Planet Fusion data will be associated with larger uncertainties during more extended gap periods (Figure A8; Figure 4). In those periods, NIRvP tracked GPP better than NIRv did, which could be explained by the role of day-to-day variations of PAR in predicting GPP. Moreover, the study sites are mostly cloud-free during the growing season, which is an ideal case, other sites might have broken clouds with shadows. In that case, the spatial mismatch between satellite-derived PAR and NIRv might degrade the performance of NIRvP-based GPP estimation as PAR with coarse spatial resolution cannot provide the radiation information separately between cloudy and cloud-free areas. In future works on cloudy areas, PAR derived from geostationary satellites with a high spatial resolution (Zhang et al., 2021) could be an option although the spatial resolution is still much coarser than the Planet Fusion imagery. Regarding *in situ* measurements, continuous eddy covariance measurements can be relatively free from outliers compared to snapshot satellite imagery but sampling errors can also lead to outliers (Figure 6, Figure S4) even after integrating samples at 20 Hz to 30-min data (Moffat et al., 2007; Richardson et al., 2006). At a

daily time scale, uncertainty (one standard deviation) in tower-derived GPP is typically assumed to be 15–20% of the measurements (Falge et al., 2002; Hagen et al., 2006; Richardson et al., 2006). Moreover, the assumptions made during the partitioning of GPP from NEE could induce uncertainty (Reichstein et al., 2005). Theoretically, both PAR and GPP should be zero in nighttime but gap-filled GPP have both negative and positive values in the nighttime due to an unideal temperature function of nighttime NEE. Therefore, the daily (0000hh-2400hh) GPP values are larger than daytime (0800hh-1800hh) GPP (Figure S9). Since we targeted to estimate daily GPP, which is needed for annual accumulated GPP, NIRvP–daily GPP relationship will be biased when we force nighttime GPP to 0 or exclude nighttime GPP in daily GPP (Figure S9). In the case of US-Snf (Pasture), the peak growing season over US-Snf (Pasture) was around December to June but the data were used from June to December in this study (Table 1). Hence, when vegetations are less active, the presence of cattle in US-Snf (Pasture), which can affect carbon dioxide fluxes (Baldocchi et al., 2012; Detto et al., 2010), might influence the relationship between NIRvP and GPP. Regarding footprint matching between Planet Fusion NIRvP and GPP, we weighted Planet Fusion pixels within the flux footprints based on the contour lines rather than the spatially fully explicit footprint contributions per pixel. Therefore, we also encourage future studies to develop pixel-based footprint model for calculating the footprint contribution per pixel.

Matching the footprint between Planet Fusion-derived NIRvP and GPP measurements enables us to use the full potential of flux tower data for spatial upscaling. Previous studies have already pointed out the importance of the spatial heterogeneity within flux tower footprints as the primary source of uncertainty in spatial upscaling (Giannico et al., 2018; Ran et al., 2016) and the role of CubeSat data in a robust spatial upscaling (Ryu et al., 2019). As Planet Fusion NIRvP could be successfully matched to the flux tower footprint (Figure 2; Appendix 2) despite frequent mowing and water extent changes (Figure 7), it could, in principle, also be used as a new tool for characterizing the heterogeneity of the eddy covariance footprints of all FLUXNET sites. The important difference to previous approaches relying on NDVI or other greenness indicators (e.g. Chen et al. (2011), Chen et al. (2012), Chu et al. (2021)) would be to use NIRv as proxy for GPP, assuming sufficiently constant PAR in the selected area. To characterize the spatial heterogeneity, one could use semi-variogram (Kim et al., 2006), which is a suitable geostatistical method for analyzing spatial patterns. Such an analysis could well lead to unexpected results as sites that were previously characterized as homogeneous landscapes (e.g., cropland) may show considerable spatial heterogeneities (Figure A8). Apart from the footprint characterization that might also be of general interest to the eddy covariance community, Planet Fusion NIRvP will allow us to also include sites with heterogeneous footprints and landcover for spatial upscaling, which have not previously been feasible as the traditional satellite products with coarser spatio- temporal resolution had to rely on a selection of homogeneous sites to avoid biased results (Chen et al., 2011; Ran et al., 2016). Although the footprint matching also improved temporal correlation of NIRvP against GPP for each site (Figure 8), it was not as much as the convergence of slopes across the

sites (Figure 7). NIRvP-based GPP estimation varied within the sites depending on the vegetation types and canopy structures but the slope of NIRvP-based daily GPP against *in situ* GPP over the study period were similar (Figure 10) because climate factors were the dominant drivers. Nevertheless, variations of NIRvP-GPP regression slopes could appear in very dense forest, ecosystems with high species diversity, and vertically heterogeneous canopies (Ishii et al., 2004), which were not tested in this study. In particular, evergreen needleleaf trees stay green during winter although their photosynthesis is nearly nil, which can lead to seasonally changing slopes between NIRvP and GPP (Kim et al., 2021).

Our results highlight the potential of CubeSat-based imagery for daily canopy GPP estimation. Previous studies have applied CubeSat datasets to monitor phenology, leaf area index, NDVI, and evapotranspiration (Aragon et al., 2018; Aragon et al., 2021; Houborg and McCabe, 2018b; Hwang et al., 2020; Kimm et al., 2020). The results of our study suggest that CubeSat imagery can be used to obtain daily canopy photosynthesis data at fine spatial and temporal resolution, thus overcoming limitations inherent in using only observations from individual sun-synchronous satellites such as MODIS and Landsat. Moreover, potential improvements of Planet Fusion -derived NIRv for NIRvP mapping have already been suggested (Jiang et al., 2021). In particular, Jiang et al. (2021) and Zeng et al. (2019) suggested methods to account for the non-zero NIRv values for bare soil or dead vegetation, which could lead to improvements in GPP estimation especially outside the main growing season. However, these approaches need additional information at each site and only can predict GPP after the current season unless assumptions are made based on previous years' data. Further studies should evaluate the performance of Planet Fusion NIRvP for an even broader range of ecosystem types in various geographical locations and physiological stress conditions including drought and flood. Incorporation of inexpensive spectral sensors into flux towers that can monitor NIRv (Garrity et al., 2010; Kim et al., 2019; Ryu et al., 2010) and using existing sensor networks to increase ground observation of NIRv across the globe (Carrer et al., 2021) will be a useful strategy for evaluating and improving CubeSat-based fine-resolution GPP mapping.

5. Conclusions

In this study, we evaluated the performance of satellite-derived NIRvP as a proxy for GPP by comparing it with *in situ* GPP from a flux tower network over a heterogeneous landscape consisting of mixed wetlands and croplands. We found that the best agreement between flux tower GPP and NIRvP calculated from the Planet Fusion-based product was achieved when matching the Planet Fusion imagery to the tower flux footprints. In fact, the agreement of Planet Fusion imagery matched to the flux tower footprint was even considerably better than the agreement between *in situ* NIRvP and tower GPP. The improvement for GPP estimation due to the flux tower footprint matching was evidenced by the higher across-site consistency in linear regression slopes between Planet Fusion NIRvP and GPP

compared to either fixed footprint Planet Fusion NIRvP or *in situ* NIRvP. This indicates a large impact of the mismatch between flux tower footprint and the area covered by optical sensors due to spatial heterogeneity within the temporally varying flux tower footprint. We found the largest effects of such mismatches in wetland sites that have a temporally varying fraction of vegetation in a given area. The performance of Planet Fusion-based NIRvP was robust across sites and times in the growing season both for GPP estimation at the time of satellite overpass and for daily summed values. Accordingly, Planet Fusion NIRvP serves as a viable metric for creating daily, high spatial resolution GPP maps at the landscape scale which could prove very useful for precision agriculture or the monitoring of heterogeneous and dynamic natural ecosystems such as wetlands. We encourage future efforts to test the proposed approach in a wide variety of ecosystems during water-limited or light saturation periods. Overall, our results demonstrated significant advantages of the high spatio-temporal resolution Planet Fusion products for daily canopy GPP estimation and for upscaling flux data for model validation and parameterization. More generally, our findings indicate the large potential of sensor data fusion for high fidelity vegetation monitoring at unprecedented spatial and temporal resolutions.

Acknowledgement

This research was funded by the National Research Foundation of Korea (NRF-2019R1A2C2084626) and the Cooperative Research Program for Agriculture Science & Technology Development (Project No. PJ01475502), Rural Development Administration, Republic of Korea. Proofreading was supported by the Research Institute of Agriculture and Life Sciences, Seoul National University. Dennis D. Baldocchi was supported by the US Department of Energy, office of science and Ameriflux and NASA Ecostress project.

Appendix

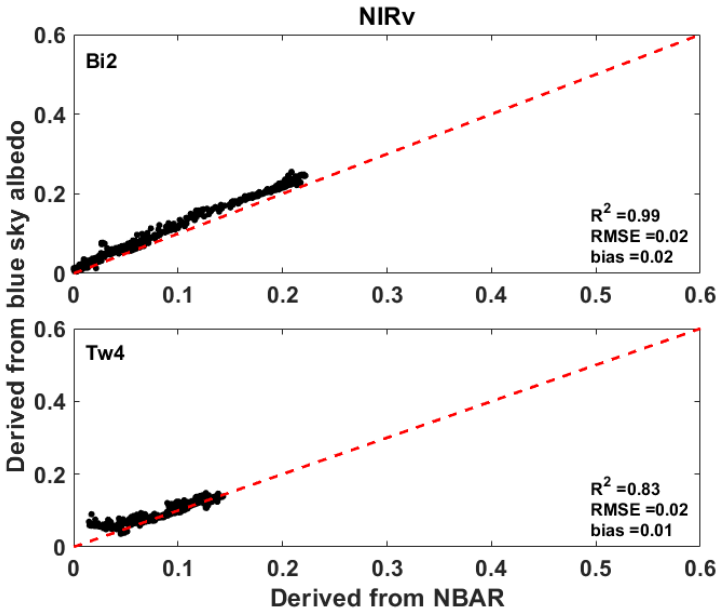

Figure A1 Evaluation of view geometry effects on *in situ* near-infrared radiation from vegetation (NIRv) from 2018 to 2019. Using MCD43A1 bidirectional reflectance distribution function parameters, we converted *in situ* bi-hemispheric reflectance into blue sky albedo at 1030hh (local time UTC-8) and compared it to a nadir bidirectional reflectance distribution function-adjusted reflectance (NBAR) product (MCD43A4).

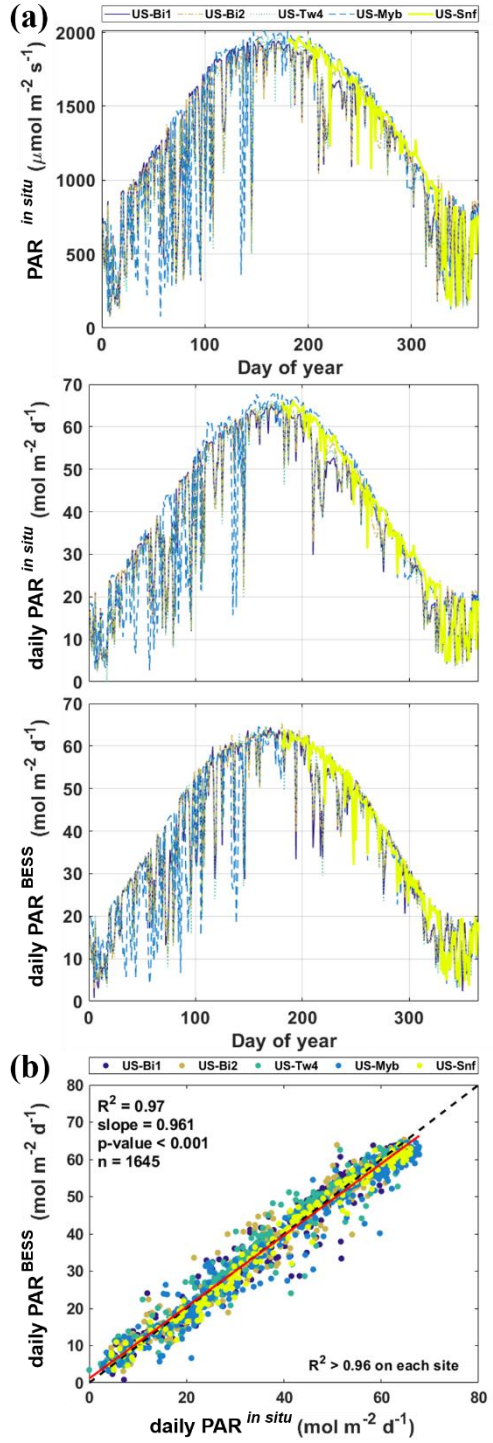

Figure A2 Evaluation of photosynthetically active radiation (PAR) data in this study. (a) Seasonal variation in PAR throughout 2018 at three sites (US-Bi1, Alfalfa; US-Bi2, Corn; and US-Tw4, Freshwater wetland) and 2019 in two sites (US-Myb, Palustrine wetland; and US-Snf, Pasture), including instantaneous *in situ* PAR at satellite passing time ($PAR^{in\ situ}_{satellite}$), *in situ* daily PAR ($PAR^{in\ situ}_{daily}$), and BESS daily PAR ($PAR^{BESS}_{daily}$). (b) The relationship between BESS daily PAR and *in situ* daily PAR. Dashed black line is a 1:1 line (y = x). Red lines indicate the slopes of the linear regression models for each site. R^2 is the coefficient of determination, p-value indicates the significance of the linear regression, and n is the number of samples used in the linear regression model. For the US-Snf site, the daily PAR value was approximately 89% lower than the mean of the other sites throughout 2019; therefore, we applied a correction factor of 1.14 to all US-Snf PAR data.

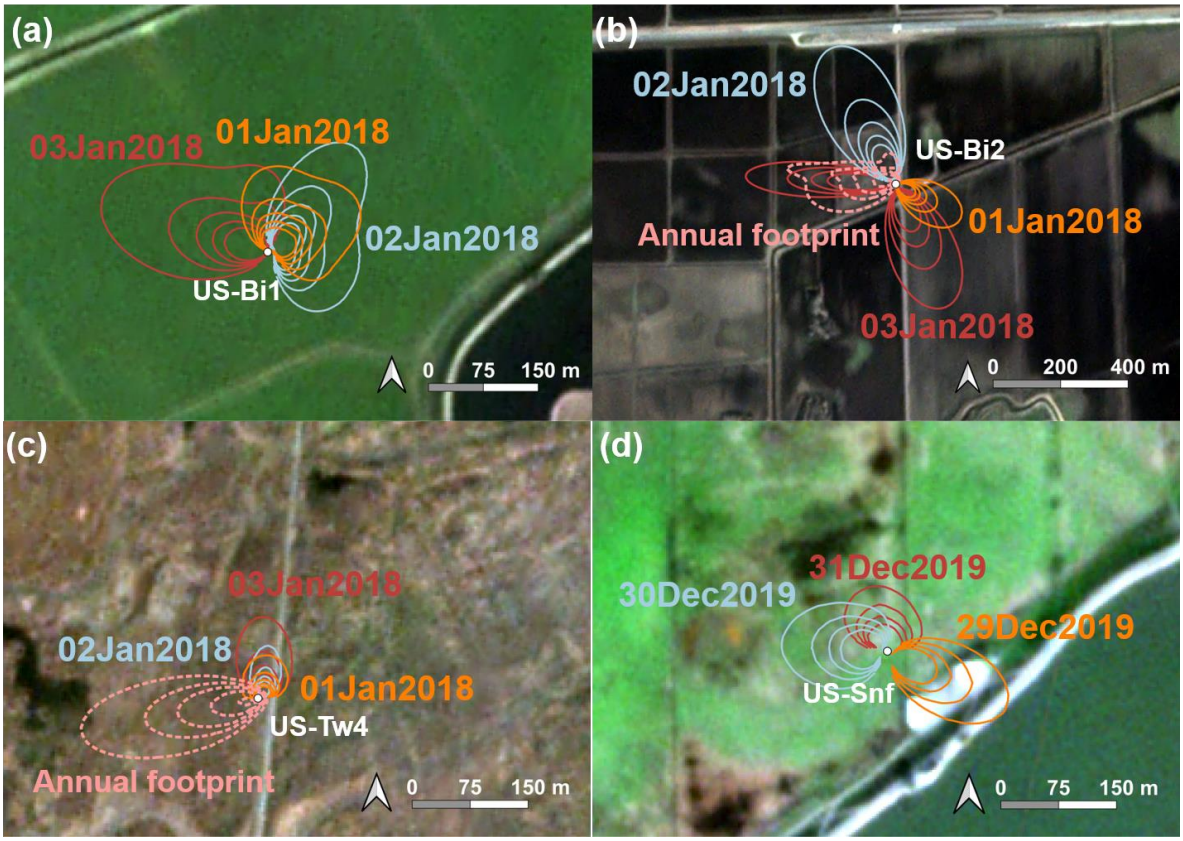

Figure A3 Examples of daily eddy covariance (EC) footprints at sites (a) US-Bi1 (Alfalfa), (b) US-Bi2 (Corn), (c) US-Tw4 (Freshwater wetland), and (d) US-Snf (Pasture) from (a–c) January 1–3, 2018 and from (d) December 29–31, 2019. Additionally, annual cumulative footprints were denoted over (a) US-Bi2 from 2017 and (c) US-Tw4 from 2016. Contour lines delineate footprints within which (a–c) 50–90% and (d) 50–80% of the cumulative flux originated. Image source: red–green–black (RGB) Planet Fusion product (projection, WGS84/UTM zone 10N) for (a–c) January 1, 2018, and (d) December 29, 2019.

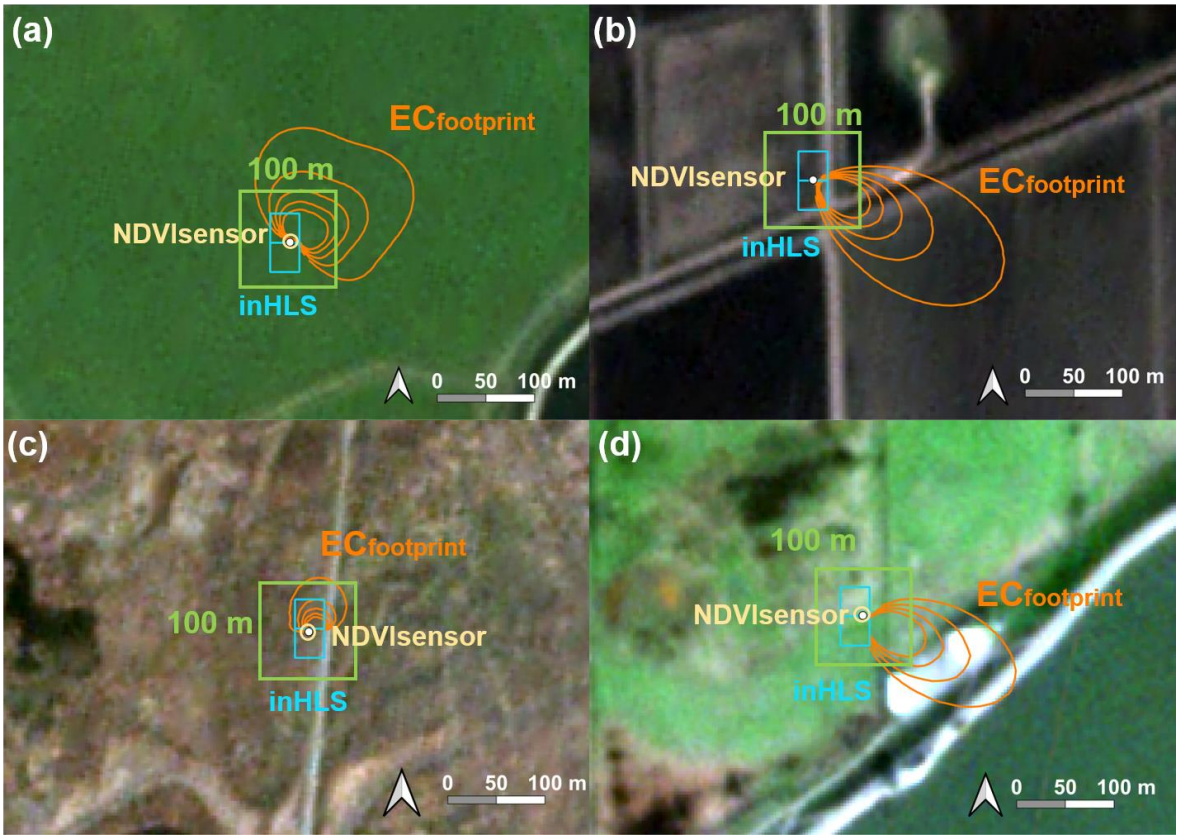

Figure A4 Examples of footprints for flux towers (white dots) at sites (a) US-Bi1 (Alfalfa), (b) US-Bi2 (Corn), (c) US-Tw4 (Freshwater wetland), and (d) US-Snf (Pasture) for different footprint types including eddy covariance footprint on January 1, 2018 (orange), a fixed 100 m × 100 m footprint (green) around the eddy covariance tower, and Harmonized Landsat/Sentinel (inHLS) pixels (cyan) including the normalized difference vegetation index (NDVI) sensor footprint (yellow). Contour lines denote the footprints within which 50–90% (a-c) and 50–80% (d) of the cumulative flux originated. Image source: RGB Planet Fusion surface reflectance product (projection, WGS84/UTM zone 10N) for (a–c) January 1, 2018, and (d) December 29, 2019.

Table A5 Comparison of NIRv and NIRvP derived from MODIS HSL, and observation-derived and gap-filled Planet Fusion (PF) data with *in situ* NIRv and NIRvP at each site. R^2, coefficient of determination; RMSE, root mean square error; rbias, relative bias; slope, slope of linear regression; n, number of samples.

Site ID	R^2	RMSE	Bias	rbias (%)	slope	R^2	RMSE	Bias	rbias (%)	slope	n
					MODIS						
			NIRv					**NIRvP**			
US-Bi1	0.42	0.09	0.05	33.0	0.38	0.82	95.80	46.26	17.7	0.73	365
US-Bi2	0.93	0.03	0.01	5.5	0.99	0.94	49.44	1.60	1.0	0.98	364
US-Tw4	0.94	0.14	0.13	368.6	2.14	0.94	221.49	196.64	322.6	2.83	313
US-Myb	0.74	0.15	0.13	294.3	2.55	0.89	259.70	216.15	280.7	3.37	338
US-Snf	0.80	0.09	0.09	104.7	0.67	0.94	124.67	118.38	82.4	1.24	185
Overall	0.44	0.11	0.08	91.9	0.66	0.51	170.07	111.17	77.8	0.81	1565
					HLS						
			NIR					**NIRvP**			
US-Bi1	0.70	0.09	0.08	37.6	1.01	0.85	131.41	107.88	32.1	1.02	50
US-Bi2	0.95	0.04	-0.02	-13.1	0.76	0.96	68.35	-34.32	-15.5	0.77	48
US-Tw4	0.84	0.11	0.11	229.6	1.54	0.92	182.68	176.36	216.4	1.80	41
US-Myb	0.52	0.02	0.01	18.5	0.91	0.64	35.22	16.50	16.1	0.95	42
US-Snf	0.75	0.07	0.06	63.1	1.02	0.91	111.82	102.89	59.0	1.30	28
Overall	0.69	0.07	0.05	41.2	0.94	0.73	116.94	69.62	36.4	0.92	209
					observed Planet Fusion						
			NIRv					**NIRvP**			
US-Bi1	0.75	0.09	0.08	39.2	1.04	0.88	126.86	107.05	33.3	1.04	177
US-Bi2	0.98	0.02	-0.01	-6.1	0.85	0.98	44.29	-17.28	-8.2	0.85	184
US-Tw4	0.83	0.10	0.10	212.7	1.71	0.94	165.68	157.50	198.1	1.94	176
US-Myb	0.81	0.01	0.01	9.4	0.69	0.92	15.62	5.95	6.3	0.81	174
US-Snf	0.90	0.05	0.05	50.1	0.71	0.98	69.76	68.14	42.1	1.01	101
Overall	0.74	0.07	0.04	41.8	0.98	0.79	102.76	63.31	36.1	0.96	812
					Gap-filled Planet Fusion						
			NIRv					**NIRvP**			
US-Bi1	0.54	0.12	0.10	59.5%	0.76	0.90	121.87	103.40	39.7	1.03	365
US-Bi2	0.98	0.02	0.00	-0.5%	0.84	0.98	36.85	-9.12	-5.9	0.85	364
US-Tw4	0.86	0.09	0.09	246.4%	1.74	0.94	143.85	128.26	210.4	2.14	313
US-Myb	0.82	0.01	0.01	18.9%	0.65	0.94	15.21	6.79	8.8	0.86	338
US-Snf	0.87	0.05	0.05	59.9%	0.65	0.97	66.06	63.24	44.0	1.07	185
Overall	0.69	0.08	0.05	55.7%	0.99	0.83	92.11	56.59	39.6	1.01	1565

Table A6 Comparison of GPP *in situ* measurements at satellite passing time with NIRv (NIRvP) derived from *in situ* measurements and Planet Fusion for different footprint types. R^2, coefficient of determination; slope, slope of linear regression; n, number of samples.

Site ID		*In situ*	$NDVI_{sensor}$	100m	$EC_{footprint}$	$EC_{footprint}$ (30 m resolution)
			NIRv			
	R^2	0.76	0.56	0.57	0.60	0.61
US-Bi1	Slope	105.33	87.26	99.58	96.45	98.22
	n	365	365	365	359	298
	R^2	0.89	0.87	0.85	0.84	0.84
US-Bi2	Slope	158.20	183.93	231.13	152.68	152.55
	n	364	365	365	355	346
	R^2	0.92	0.87	0.88	0.88	0.93
US-Tw4	Slope	343.22	171.18	189.37	184.91	163.77
	n	313	365	365	354	66
	R^2	0.69	0.59	0.57	0.81	0.77
US-Myb	Slope	263.12	327.34	186.86	123.12	119.92
	n	338	365	365	360	274
	R^2	0.82	0.80	0.87	0.77	0.63
US-Snf	Slope	138.70	195.73	197.28	163.16	157.66
	n	185	185	185	181	132
	R^2	0.58	0.43	0.46	0.62	0.64
Overall	Slope	105.98	76.43	94.85	101.59	99.78
	n	1565	1645	1645	1609	1116
			NIRvP			
	R^2	0.71	0.78	0.79	0.80	0.81
US-Bi1	Slope	0.05	0.05	0.05	0.05	0.05
	n	365	365	365	359	298
	R^2	0.88	0.87	0.86	0.86	0.86
US-Bi2	Slope	0.09	0.10	0.12	0.08	0.08
	n	364	365	365	355	346
	R^2	0.87	0.91	0.86	0.89	0.83
US-Tw4	Slope	0.18	0.08	0.08	0.08	0.06
	n	313	364	364	354	66
	R^2	0.84	0.83	0.83	0.92	0.90
US-Myb	Slope	0.14	0.15	0.09	0.06	0.06
	n	338	365	365	360	274
	R^2	0.83	0.85	0.85	0.88	0.85
US-Snf	Slope	0.06	0.06	0.06	0.06	0.06
	n	185	185	185	181	132
	R^2	0.61	0.61	0.65	0.78	0.78
Overall	Slope	0.06	0.05	0.06	0.06	0.06
	n	1565	1644	1644	1609	1116

Table A7 Comparison of *in situ* daily GPP measurements with daily NIRvP and NIRv × PAR_{daily}^{BESS} for all sites.

Site ID		Daily NIRvP		NIRv x PAR_{daily}^{BESS}	
		$NIRvP^{in\ situ}$	$NIRvP_{ECfootprint}^{PF}$	*In situ*	Planet Fusion
US-Bi1	R^2	0.80	0.82	0.79	0.80
	Slope	0.80	0.67	0.68	0.69
	RMSE	2.33	4.51	3.21	4.24
	n	365	359	365	359
US-Bi2	R^2	0.86	0.83	0.85	0.82
	Slope	1.17	0.98	1.02	1.01
	RMSE	2.62	2.80	2.63	2.83
	n	365	355	364	355
US-Tw4	R^2	0.90	0.91	0.90	0.89
	Slope	2.32	0.94	2.35	1.00
	RMSE	4.03	1.51	4.15	1.48
	n	341	354	313	354
US-Myb	R^2	0.90	0.92	0.85	0.92
	Slope	1.87	0.74	1.96	0.81
	RMSE	3.13	1.56	3.29	1.24
	n	339	360	338	360
US-Snf	R^2	0.83	0.85	0.83	0.84
	Slope	0.86	0.67	0.78	0.70
	RMSE	1.13	2.85	1.37	2.56
	n	185	181	185	181
Overall	R^2	0.67	0.80	0.62	0.79
	Slope	0.91	0.77	0.76	0.80
	RMSE	2.68	2.08	2.88	2.15
	n	1595	1609	1565	1609

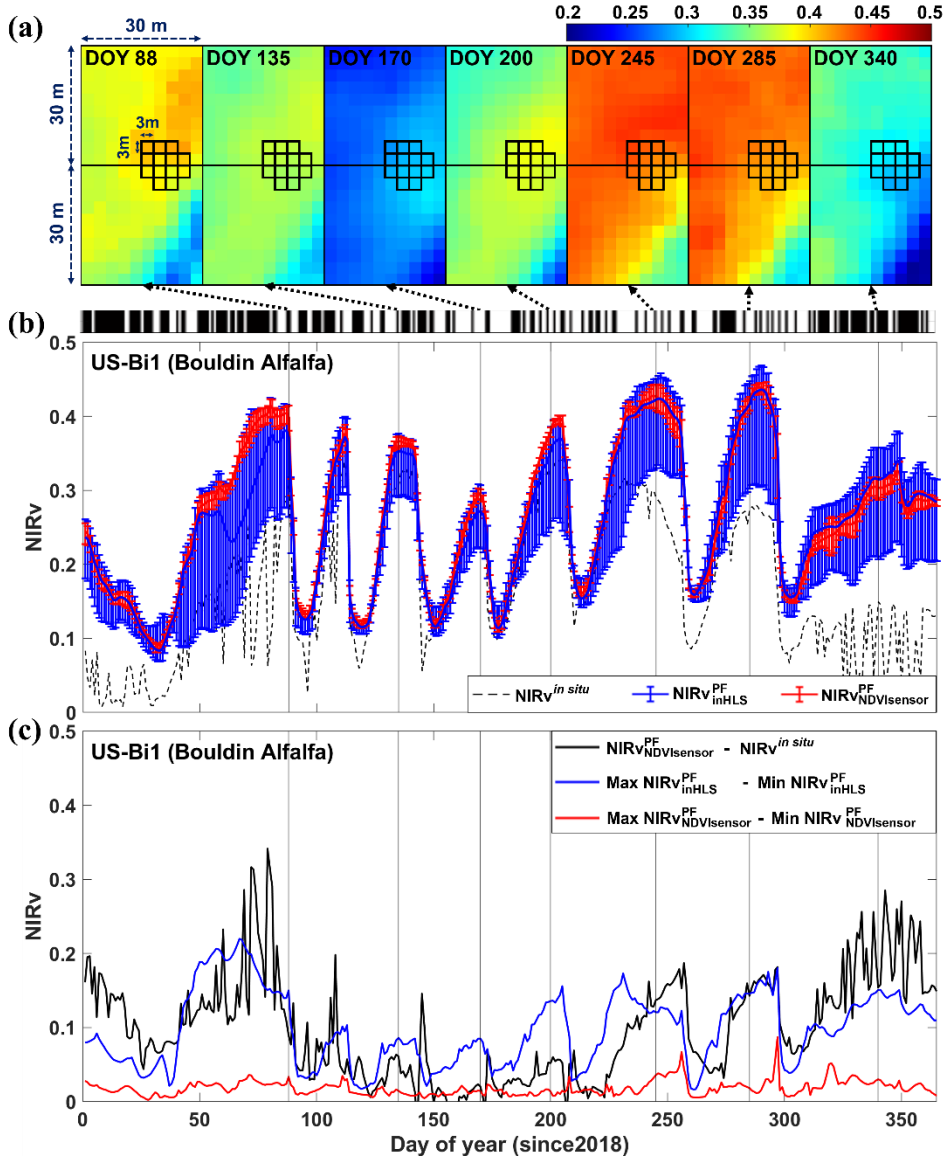

Figure A8 (a) Spatial variation in Planet Fusion (PF) NIRv in inHLS footprints, which comprised two 30 m × 30 m boxes, and $NDVI_{sensor}$ footprints, which comprised 13 black boxes (3 m × 3 m in size) at site US-Bi1 (Alfalfa). (b) Seasonal variation in NIRv at site US-Bi1, derived from Planet Fusion with $NDVI_{sensor}$ footprint (red line), Planet Fusion with inHLS footprint (blue line), and *in situ* sensor (black dashed line), where black lines on top of the plot indicate gap-filled data. Vertical lines indicate mean, maximum, and minimum values for $NIRv^{PF}_{NDVIsensor}$ and $NIRv^{PF}_{inHLS}$ data. (c) Differences between $NIRv^{PF}_{NDVIsensor}$ and $NIRv^{in\ situ}$ (black line). Blue and red lines indicate differences between maximum and minimum $NIRv^{PF}_{inHLS}$ and $NIRv^{PF}_{NDVIsensor}$, respectively. NIRv is given in unitless.

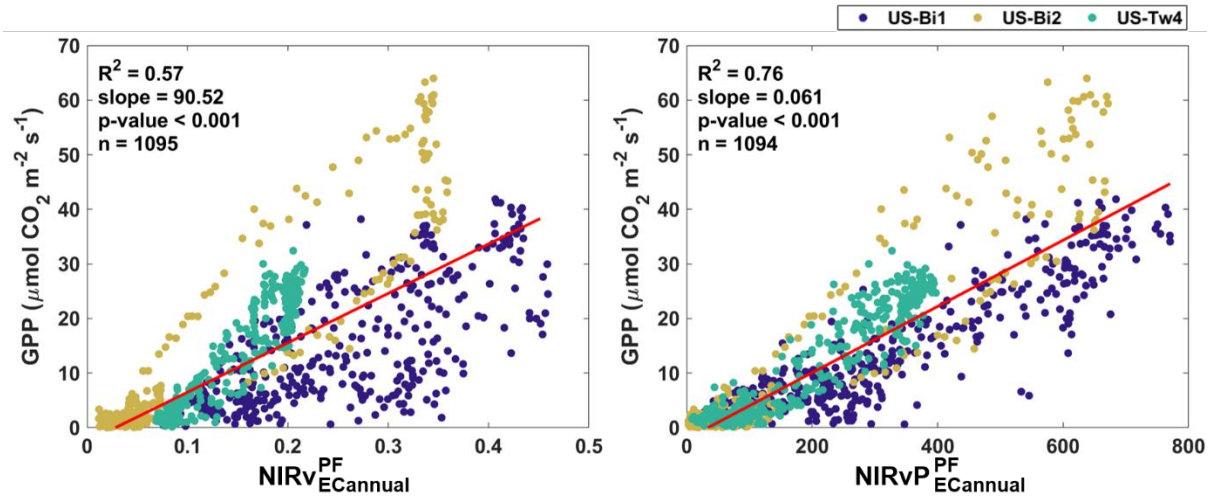

Figure A9 Comparison of NIRv and NIRvP measured derived from Planet Fusion (PF) in the annual cumulated eddy covariance footprint ($NIRv(NIRvP)^{PF}_{ECannual}$) with GPP measured in study sites (colored circles) around satellite overpassing time. Red lines indicate linear regression model slopes for all sites. R^2 is the coefficient of determination, p-value indicates the significance of the linear regression, and n is the number of samples used in the linear regression model. We assumed that the shape of the cumulative footprint over US-Bi1 (Alfalfa) is similar to that over the nearby cropland site (i.e., US-Bi2, Corn), and we considered the inter-annual variations of cumulative footprints were small. The annual cumulative footprint over US-Tw4 (Freshwater wetland) (2016) and US-Bi2 (2017) were used (Figure A3). NIRv and NIRvP are given in unitless and unit of μmol m^{-2} s^{-1} , respectively.

References

Alexandrov, T., 2009. A Method of Trend Extraction Using Singular Spectrum Analysis. REVSTAT – Statistical Journa, 7.

Aragon, B., Houborg, R., Tu, K., Fisher, J.B. and McCabe, M., 2018. CubeSats Enable High Spatiotemporal Retrievals of Crop-Water Use for Precision Agriculture. Remote Sensing, 10(12): 1867,https://doi.org/10.3390/rs10121867.

Aragon, B., Ziliani, M.G., Houborg, R., Franz, T.E. and McCabe, M.F., 2021. CubeSats deliver new insights into agricultural water use at daily and 3 m resolutions. Scientific Reports, 11(1): 12131,https://doi.org/10.1038/s41598-021-91646-w.

Badgley, G., Anderegg, L.D.L., Berry, J.A. and Field, C.B., 2019. Terrestrial gross primary production: Using NIRV to scale from site to globe. Global Change Biology, 25(11): 3731-3740,https://doi.org/10.1111/gcb.14729.

Badgley, G., Field, C.B. and Berry, J.A., 2017. Canopy near-infrared reflectance and terrestrial photosynthesis. Science Advances, 3(3): e1602244,https://doi.org/10.1126/sciadv.1602244.

Baldocchi, D. et al., 2012. The challenges of measuring methane fluxes and concentrations over a peatland pasture. Agricultural and Forest Meteorology, 153: 177-187,https://doi.org/10.1016/j.agrformet.2011.04.013.

Baldocchi, D. et al., 2001. FLUXNET: A New Tool to Study the Temporal and Spatial Variability of Ecosystem-Scale Carbon Dioxide, Water Vapor, and Energy Flux Densities. Bulletin of the American Meteorological Society, 82(11): 2415-2434,https://doi.org/10.1175/1520-0477(2001)082<2415:Fantts>2.3.Co;2.

Baldocchi, D.D. et al., 2020. Outgoing Near-Infrared Radiation From Vegetation Scales With Canopy Photosynthesis Across a Spectrum of Function, Structure, Physiological Capacity, and Weather. Journal of Geophysical Research: Biogeosciences, 125(7): e2019JG005534,https://doi.org/10.1029/2019jg005534.

Carrer, D. et al., 2021. Casual Rerouting of AERONET Sun/Sky Photometers: Toward a New Network of Ground Measurements Dedicated to the Monitoring of Surface Properties? Remote Sensing, 13(16): 3072,https://doi.org/10.3390/rs13163072.

Chamberlain, S.D. et al., 2018. Soil properties and sediment accretion modulate methane fluxes from restored wetlands. Global Change Biology, 24(9): 4107-4121,https://doi.org/10.1111/gcb.14124.

Chen, B. et al., 2009. Assessing Tower Flux Footprint Climatology and Scaling Between Remotely Sensed and Eddy Covariance Measurements. Boundary-Layer Meteorology, 130(2): 137-167,https://doi.org/10.1007/s10546-008-9339-1.

Chen, B., Chen, L., Huang, B., Michishita, R. and Xu, B., 2018. Dynamic monitoring of the Poyang Lake wetland by integrating Landsat and MODIS observations. ISPRS Journal of Photogrammetry and Remote Sensing, 139: 75-87,https://doi.org/10.1016/j.isprsjprs.2018.02.021.

Chen, B. et al., 2011. Assessing eddy-covariance flux tower location bias across the Fluxnet-Canada Research Network based on remote sensing and footprint modelling. Agricultural and Forest Meteorology, 151(1): 87-100,https://doi.org/10.1016/j.agrformet.2010.09.005.

Chen, B. et al., 2012. Characterizing spatial representativeness of flux tower eddy-covariance measurements across the Canadian Carbon Program Network using remote sensing and footprint analysis. Remote Sensing of Environment, 124: 742-755,https://doi.org/10.1016/j.rse.2012.06.007.

Chu, H. et al., 2018. Temporal Dynamics of Aerodynamic Canopy Height Derived From Eddy Covariance Momentum Flux Data Across North American Flux Networks. Geophysical Research Letters, 45(17):

9275-9287,https://doi.org/10.1029/2018GL079306.

Chu, H. et al., 2021. Representativeness of Eddy-Covariance flux footprints for areas surrounding AmeriFlux sites. Agricultural and Forest Meteorology, 301-302: 108350,https://doi.org/10.1016/j.agrformet.2021.108350.

Ciais, P. et al., 2014. Current systematic carbon-cycle observations and the need for implementing a policy-relevant carbon observing system. Biogeosciences, 11(13): 3547-3602,https://doi.org/10.5194/bg-11-3547-2014.

Claverie, M. et al., 2018. The Harmonized Landsat and Sentinel-2 surface reflectance data set. Remote Sensing of Environment, 219: 145-161,https://doi.org/10.1016/j.rse.2018.09.002.

Dechant, B. et al., 2022. NIRVP: A robust structural proxy for sun-induced chlorophyll fluorescence and photosynthesis across scales. Remote Sensing of Environment, 268: 112763,https://doi.org/10.1016/j.rse.2021.112763.

Dechant, B. et al., 2020. Canopy structure explains the relationship between photosynthesis and sun-induced chlorophyll fluorescence in crops. Remote Sensing of Environment, 241: 111733,https://doi.org/10.1016/j.rse.2020.111733.

Dechant, B., Ryu, Y. and Kang, M., 2019. Making full use of hyperspectral data for gross primary productivity estimation with multivariate regression: Mechanistic insights from observations and process-based simulations. Remote Sensing of Environment, 234: 111435,https://doi.org/10.1016/j.rse.2019.111435.

Detto, M., Baldocchi, D. and Katul, G.G., 2010. Scaling Properties of Biologically Active Scalar Concentration Fluctuations in the Atmospheric Surface Layer over a Managed Peatland. Boundary-Layer Meteorology, 136(3): 407-430,https://doi.org/10.1007/s10546-010-9514-z.

Drusch, M. et al., 2012. Sentinel-2: ESA's Optical High-Resolution Mission for GMES Operational Services. Remote Sensing of Environment, 120: 25-36,https://doi.org/10.1016/j.rse.2011.11.026.

Duveiller, G. and Defourny, P., 2010. A conceptual framework to define the spatial resolution requirements for agricultural monitoring using remote sensing. Remote Sensing of Environment, 114(11): 2637-2650,https://doi.org/10.1016/j.rse.2010.06.001.

Eichelmann, E. et al., 2018. The effect of land cover type and structure on evapotranspiration from agricultural and wetland sites in the Sacramento–San Joaquin River Delta, California. Agricultural and Forest Meteorology, 256-257: 179-195,https://doi.org/10.1016/j.agrformet.2018.03.007.

Eichelmann, E. et al., 2021. AmeriFlux US-Tw4 Twitchell East End Wetland, Ver. 11-5. AmeriFlux AMP,https://doi.org/10.17190/AMF/1246151.

Falge, E. et al., 2002. Seasonality of ecosystem respiration and gross primary production as derived from FLUXNET measurements. Agricultural and Forest Meteorology, 113(1): 53-74,https://doi.org/10.1016/S0168-1923(02)00102-8.

Federer, C.A., 1968. Spatial Variation of Net Radiation, Albedo and Surface Temperature of Forests. Journal of Applied Meteorology and Climatology, 7(5): 789-795,https://doi.org/10.1175/1520-0450(1968)007<0789:SVONRA>2.0.CO;2.

Fisher, J.B. et al., 2020. ECOSTRESS: NASA's Next Generation Mission to Measure Evapotranspiration From the International Space Station. Water Resources Research, 56(4): e2019WR026058,https://doi.org/10.1029/2019WR026058.

Frantz, D., 2019. FORCE—Landsat + Sentinel-2 Analysis Ready Data and Beyond. Remote Sensing, 11(9),https://doi.org/10.3390/rs11091124.

Gamon, J.A., 2015. Reviews and Syntheses: optical sampling of the flux tower footprint. Biogeosciences, 12(14): 4509-4523,https://doi.org/10.5194/bg-12-4509-2015.

Garrity, S.R., Vierling, L.A. and Bickford, K., 2010. A simple filtered photodiode instrument for continuous measurement of narrowband NDVI and PRI over vegetated canopies. Agricultural and Forest Meteorology, 150(3): 489-496,https://doi.org/10.1016/j.agrformet.2010.01.004.

Ghil, M. et al., 2002. ADVANCED SPECTRAL METHODS FOR CLIMATIC TIME SERIES. Reviews of Geophysics, 40(1): 3-1-3-41,https://doi.org/10.1029/2000RG000092.

Giannico, V. et al., 2018. Contributions of landscape heterogeneity within the footprint of eddy-covariance towers to flux measurements. Agricultural and Forest Meteorology, 260-261: 144-153,https://doi.org/10.1016/j.agrformet.2018.06.004.

Golyandina, N., Korobeynikov, A. and Zhigljavsky, A., 2018. Singular spectrum analysis with R. Springer.

Hagen, S.C. et al., 2006. Statistical uncertainty of eddy flux–based estimates of gross ecosystem carbon exchange at Howland Forest, Maine. Journal of Geophysical Research: Atmospheres, 111(D8),https://doi.org/10.1029/2005JD006154.

Halabisky, M., Moskal, L.M., Gillespie, A. and Hannam, M., 2016. Reconstructing semi-arid wetland surface water dynamics through spectral mixture analysis of a time series of Landsat satellite images (1984–2011). Remote Sensing of Environment, 177: 171-183,https://doi.org/10.1016/j.rse.2016.02.040.

Heinsch, F.A. et al., 2006. Evaluation of remote sensing based terrestrial productivity from MODIS using regional tower eddy flux network observations. IEEE Transactions on Geoscience and Remote Sensing, 44(7): 1908-1925,https://doi.org/10.1109/TGRS.2005.853936.

Helder, D. et al., 2020. Observations and Recommendations for Coordinated Calibration Activities of Government and Commercial Optical Satellite Systems. Remote Sensing, 12(15),https://doi.org/10.3390/rs12152468.

Hemes, K.S. et al., 2019. Assessing the carbon and climate benefit of restoring degraded agricultural peat soils to managed wetlands. Agricultural and Forest Meteorology, 268: 202-214,https://doi.org/10.1016/j.agrformet.2019.01.017.

Hemes, K.S., Verfaillie, J. and Baldocchi, D.D., 2020. Wildfire-Smoke Aerosols Lead to Increased Light Use Efficiency Among Agricultural and Restored Wetland Land Uses in California's Central Valley. Journal of Geophysical Research: Biogeosciences, 125(2): e2019JG005380,https://doi.org/10.1029/2019JG005380.

Houborg, R. and McCabe, M.F., 2016. High-Resolution NDVI from Planet's Constellation of Earth Observing Nano-Satellites: A New Data Source for Precision Agriculture. Remote Sensing, 8(9),https://doi.org/10.3390/rs8090768.

Houborg, R. and McCabe, M.F., 2018a. A Cubesat enabled Spatio-Temporal Enhancement Method (CESTEM) utilizing Planet, Landsat and MODIS data. Remote Sensing of Environment, 209: 211-226,https://doi.org/10.1016/j.rse.2018.02.067.

Houborg, R. and McCabe, M.F., 2018b. Daily Retrieval of NDVI and LAI at 3 m Resolution via the Fusion of CubeSat, Landsat, and MODIS Data. Remote Sensing, 10(6): 890,https://doi.org/10.3390/rs10060890.

Hwang, Y. et al., 2020. Comprehensive assessments of carbon dynamics in an intermittently-irrigated rice paddy. Agricultural and Forest Meteorology, 285-286: 107933,https://doi.org/10.1016/j.agrformet.2020.107933.

Ishii, H.T., Tanabe, S.-i. and Hiura, T., 2004. Exploring the Relationships Among Canopy Structure, Stand Productivity, and Biodiversity of Temperate Forest Ecosystems. Forest Science, 50(3): 342-355,https://doi.org/10.1093/forestscience/50.3.342.

Jiang, C., Guan, K., Wu, G., Peng, B. and Wang, S., 2021. A daily, 250m and real-time gross primary productivity product (2000–present) covering the contiguous United States. Earth Syst. Sci. Data, 13(2): 281-298,https://doi.org/10.5194/essd-13-281-2021.

Justice, C.O. et al., 1998. The Moderate Resolution Imaging Spectroradiometer (MODIS): land remote sensing for global change research. IEEE Transactions on Geoscience and Remote Sensing, 36(4): 1228-1249,https://doi.org/10.1109/36.701075.

Kasak, K. et al., 2021. Restoring wetlands on intensive agricultural lands modifies nitrogen cycling microbial communities and reduces N2O production potential. Journal of Environmental Management, 299: 113562,https://doi.org/10.1016/j.jenvman.2021.113562.

Kasak, K. et al., 2020. Experimental harvesting of wetland plants to evaluate trade-offs between reducing methane emissions and removing nutrients accumulated to the biomass in constructed wetlands. Science of The Total Environment, 715: 136960,https://doi.org/10.1016/j.scitotenv.2020.136960.

Khan, A.M. et al., 2021. Reviews and syntheses: Ongoing and emerging opportunities to improve environmental science using observations from the Advanced Baseline Imager on the Geostationary Operational Environmental Satellites. Biogeosciences, 18(13): 4117-4141,https://doi.org/10.5194/bg-18-4117-2021.

Kim, J. et al., 2006. Upscaling fluxes from tower to landscape: Overlaying flux footprints on high-resolution (IKONOS) images of vegetation cover. Agricultural and Forest Meteorology, 136(3): 132-146,https://doi.org/10.1016/j.agrformet.2004.11.015.

Kim, J. et al., 2021. Solar-induced chlorophyll fluorescence is non-linearly related to canopy photosynthesis in a temperate evergreen needleleaf forest during the fall transition. Remote Sensing of Environment, 258: 112362,https://doi.org/10.1016/j.rse.2021.112362.

Kim, J., Ryu, Y., Jiang, C. and Hwang, Y., 2019. Continuous observation of vegetation canopy dynamics using an integrated low-cost, near-surface remote sensing system. Agricultural and Forest Meteorology, 264: 164-177,https://doi.org/10.1016/j.agrformet.2018.09.014.

Kimm, H. et al., 2021. A physiological signal derived from sun-induced chlorophyll fluorescence quantifies crop physiological response to environmental stresses in the U.S. Corn Belt. Environmental Research Letters.

Kimm, H. et al., 2020. Deriving high-spatiotemporal-resolution leaf area index for agroecosystems in the U.S. Corn Belt using Planet Labs CubeSat and STAIR fusion data. Remote Sensing of Environment, 239: 111615,https://doi.org/10.1016/j.rse.2019.111615.

Kljun, N., Calanca, P., Rotach, M.W. and Schmid, H.P., 2015. A simple two-dimensional parameterisation for Flux Footprint Prediction (FFP). Geosci. Model Dev., 8(11): 3695-3713,https://doi.org/10.5194/gmd-8-3695-2015.

Knox, S.H. et al., 2015. Agricultural peatland restoration: effects of land-use change on greenhouse gas (CO2 and CH4) fluxes in the Sacramento-San Joaquin Delta. Global Change Biology, 21(2): 750-765,https://doi.org/10.1111/gcb.12745.

Kobayashi, H. and Iwabuchi, H., 2008. A coupled 1-D atmosphere and 3-D canopy radiative transfer model for canopy reflectance, light environment, and photosynthesis simulation in a heterogeneous landscape. Remote Sensing of Environment, 112(1): 173-185,https://doi.org/10.1016/j.rse.2007.04.010.

Kong, J. et al., 2021. Evaluation of four image fusion NDVI products against in-situ spectral-measurements over a heterogeneous rice paddy landscape. Agricultural and Forest Meteorology, 297: 108255,https://doi.org/10.1016/j.agrformet.2020.108255.

Kormann, R. and Meixner, F.X., 2001. An Analytical Footprint Model For Non-Neutral Stratification. Boundary-Layer Meteorology, 99(2): 207-224,10.1023/A:1018991015119.

Kumari, S., Kambhammettu, B.V.N.P. and Niyogi, D., 2020. Sensitivity of Analytical Flux Footprint Models in Diverse Source-Receptor Configurations: A Field Experimental Study. Journal of Geophysical Research: Biogeosciences, 125(8): e2020JG005694,https://doi.org/10.1029/2020JG005694.

Kusak, K., Rey-Sanchez, C., Szutu, D. and Baldocchi, D., 2020. AmeriFlux US-Snf Sherman Barn, Ver. 3-5.

AmeriFlux AMP,https://doi.org/10.17190/AMF/1579718.

Li, F., Kustas, W.P., Anderson, M.C., Prueger, J.H. and Scott, R.L., 2008. Effect of remote sensing spatial resolution on interpreting tower-based flux observations. Remote Sensing of Environment, 112(2): 337-349,https://doi.org/10.1016/j.rse.2006.11.032.

Li, X., Xiao, J., Fisher, J.B. and Baldocchi, D.D., 2021. ECOSTRESS estimates gross primary production with fine spatial resolution for different times of day from the International Space Station. Remote Sensing of Environment, 258: 112360,https://doi.org/10.1016/j.rse.2021.112360.

Liang, S. et al., 2019. Evaluating the Spatial Representativeness of the MODerate Resolution Image Spectroradiometer Albedo Product (MCD43) at AmeriFlux Sites. Remote sensing., 11(5): 547,https://doi.org/10.3390/rs11050547.

Liu, L. et al., 2020. Estimating Maize GPP using Near-infrared Radiance of Vegetation. Science of Remote Sensing: 100009,https://doi.org/10.1016/j.srs.2020.100009.

Liu, X., Liu, L., Hu, J. and Du, S., 2017. Modeling the Footprint and Equivalent Radiance Transfer Path Length for Tower-Based Hemispherical Observations of Chlorophyll Fluorescence. Sensors (Basel), 17(5): 1131,https://doi.org/10.3390/s17051131.

Luo, Y., Guan, K. and Peng, J., 2018. STAIR: A generic and fully-automated method to fuse multiple sources of optical satellite data to generate a high-resolution, daily and cloud-/gap-free surface reflectance product. Remote Sensing of Environment, 214: 87-99,https://doi.org/10.1016/j.rse.2018.04.042.

Mahecha, M.D. et al., 2007. Characterizing ecosystem-atmosphere interactions from short to interannual time scales. Biogeosciences, 4(5): 743-758,https://doi.org/10.5194/bg-4-743-2007.

Marcolla, B. and Cescatti, A., 2018. Geometry of the hemispherical radiometric footprint over plant canopies. Theoretical and Applied Climatology, 134(3): 981-990,https://doi.org/10.1007/s00704-017-2326-z.

Matthes, J.H. et al., 2021. AmeriFlux US-Myb Mayberry Wetland, Ver. 12-5. AmeriFlux AMP,https://doi.org/10.17190/AMF/1246139.

Matthes, J.H., Sturtevant, C., Verfaillie, J., Knox, S. and Baldocchi, D., 2014. Parsing the variability in CH4 flux at a spatially heterogeneous wetland: Integrating multiple eddy covariance towers with high-resolution flux footprint analysis. Journal of Geophysical Research: Biogeosciences, 119(7): 1322-1339,https://doi.org/10.1002/2014jg002642.

McCombs, A.G., Hiscox, A.L. and Suyker, A.E., 2019. Point-to-Grid Conversion in Flux Footprints: Implications of Method Choice and Spatial Resolution for Regional-Scale Studies. Boundary-Layer Meteorology, 172(3): 457-479,https://doi.org/10.1007/s10546-019-00455-2.

Moffat, A.M. et al., 2007. Comprehensive comparison of gap-filling techniques for eddy covariance net carbon fluxes. Agricultural and Forest Meteorology, 147(3): 209-232,https://doi.org/10.1016/j.agrformet.2007.08.011.

Pastorello, G. et al., 2020. The FLUXNET2015 dataset and the ONEFlux processing pipeline for eddy covariance data. Scientific Data, 7(1): 225,https://doi.org/10.1038/s41597-020-0534-3.

Pennypacker, S. and Baldocchi, D., 2016. Seeing the Fields and Forests: Application of Surface-Layer Theory and Flux-Tower Data to Calculating Vegetation Canopy Height. Boundary-Layer Meteorology, 158(2): 165-182,https://doi.org/10.1007/s10546-015-0090-0.

Planet Fusion Team, 2021. Planet Fusion Monitoring Technical Specification, Version 1.0.0-beta.3. San Francisco, CA., https://assets.planet.com/docs/Planet_fusion_specification_March_2021.pdf.

Prabha, T.V., Leclerc, M.Y. and Baldocchi, D., 2008. Comparison of In-Canopy Flux Footprints between Large-Eddy Simulation and the Lagrangian Simulation. Journal of Applied Meteorology and Climatology, 47(8):

2115-2128,https://doi.org/10.1175/2008jamc1814.1.

Qiao, K., Zhu, W., Xie, Z. and Li, P., 2019. Estimating the Seasonal Dynamics of the Leaf Area Index Using Piecewise LAI-VI Relationships Based on Phenophases. Remote Sensing, 11(6): 689.

Ran, Y. et al., 2016. Spatial representativeness and uncertainty of eddy covariance carbon flux measurements for upscaling net ecosystem productivity to the grid scale. Agricultural and Forest Meteorology, 230-231: 114-127,https://doi.org/10.1016/j.agrformet.2016.05.008.

Reichstein, M. et al., 2005. On the separation of net ecosystem exchange into assimilation and ecosystem respiration: review and improved algorithm. Global Change Biology, 11(9): 1424-1439,https://doi.org/10.1111/j.1365-2486.2005.001002.x.

Rey-Sanchez, C. et al., in prep. Assessing Methane Emission Hotspots using Footprint-Weighed Flux maps. To be submitted to Journal of Geophysical Research: Biogeosciences.

Rey-Sanchez, C., Szutu, D., Hemes, K., Verfaillie, J. and Baldocchi, D., 2021a. AmeriFlux US-Bi2 Bouldin Island corn, Ver. 11-5. AmeriFlux AMP,https://doi.org/10.17190/AMF/1419513.

Rey-Sanchez, C. et al., 2021b. AmeriFlux US-Bi1 Bouldin Island Alfalfa, Ver. 5-5. AmeriFlux AMP,https://doi.org/10.17190/AMF/1480317.

Rey-Sanchez, C. et al., 2021c. Evaluation of Atmospheric Boundary Layer Height From Wind Profiling Radar and Slab Models and Its Responses to Seasonality of Land Cover, Subsidence, and Advection. Journal of Geophysical Research: Atmospheres, 126(7): e2020JD033775,https://doi.org/10.1029/2020JD033775.

Richardson, A.D. et al., 2006. A multi-site analysis of random error in tower-based measurements of carbon and energy fluxes. Agricultural and Forest Meteorology, 136(1): 1-18,https://doi.org/10.1016/j.agrformet.2006.01.007.

Roy, D.P., Huang, H., Houborg, R. and Martins, V.S., 2021. A global analysis of the temporal availability of PlanetScope high spatial resolution multi-spectral imagery. Remote Sensing of Environment, 264: 112586,https://doi.org/10.1016/j.rse.2021.112586.

Roy, D.P. et al., 2014. Landsat-8: Science and product vision for terrestrial global change research. Remote Sensing of Environment, 145: 154-172,https://doi.org/10.1016/j.rse.2014.02.001.

Ryu, Y. et al., 2012. On the temporal upscaling of evapotranspiration from instantaneous remote sensing measurements to 8-day mean daily-sums. Agricultural and Forest Meteorology, 152: 212-222,https://doi.org/10.1016/j.agrformet.2011.09.010.

Ryu, Y. et al., 2011. Integration of MODIS land and atmosphere products with a coupled-process model to estimate gross primary productivity and evapotranspiration from 1 km to global scales. Global Biogeochemical Cycles, 25(4),https://doi.org/10.1029/2011GB004053.

Ryu, Y. et al., 2010. Testing the performance of a novel spectral reflectance sensor, built with light emitting diodes (LEDs), to monitor ecosystem metabolism, structure and function. Agricultural and Forest Meteorology, 150(12): 1597-1606,https://doi.org/10.1016/j.agrformet.2010.08.009.

Ryu, Y., Berry, J.A. and Baldocchi, D.D., 2019. What is global photosynthesis? History, uncertainties and opportunities. Remote Sensing of Environment, 223: 95-114,https://doi.org/10.1016/j.rse.2019.01.016.

Ryu, Y., Jiang, C., Kobayashi, H. and Detto, M., 2018. MODIS-derived global land products of shortwave radiation and diffuse and total photosynthetically active radiation at 5km resolution from 2000. Remote Sensing of Environment, 204: 812-825,https://doi.org/10.1016/j.rse.2017.09.021.

Schaaf, C.B. et al., 2002. First operational BRDF, albedo nadir reflectance products from MODIS. Remote Sensing of Environment, 83(1): 135-148,https://doi.org/10.1016/S0034-4257(02)00091-3.

Schimel, D. et al., 2015. Observing terrestrial ecosystems and the carbon cycle from space. Global Change Biology, 21(5): 1762-1776,https://doi.org/10.1111/gcb.12822.

Schmid, H.P., 1997. Experimental design for flux measurements: matching scales of observations and fluxes. Agricultural and Forest Meteorology, 87(2): 179-200,https://doi.org/10.1016/S0168-1923(97)00011-7.

Valach, A.C. et al., 2021. Productive wetlands restored for carbon sequestration quickly become net CO2 sinks with site-level factors driving uptake variability. PLOS ONE, 16(3): e0248398,https://doi.org/10.1371/journal.pone.0248398.

Verma, M. et al., 2015. Improving the performance of remote sensing models for capturing intra- and inter-annual variations in daily GPP: An analysis using global FLUXNET tower data. Agricultural and Forest Meteorology, 214-215: 416-429,https://doi.org/10.1016/j.agrformet.2015.09.005.

Wang, X., Chen, J.M. and Ju, W., 2020. Photochemical reflectance index (PRI) can be used to improve the relationship between gross primary productivity (GPP) and sun-induced chlorophyll fluorescence (SIF). Remote Sensing of Environment, 246: 111888,https://doi.org/10.1016/j.rse.2020.111888.

Weiss, D.J. and Crabtree, R.L., 2011. Percent surface water estimation from MODIS BRDF 16-day image composites. Remote Sensing of Environment, 115(8): 2035-2046,https://doi.org/10.1016/j.rse.2011.04.005.

Wu, G. et al., 2020. Radiance-based NIRv as a proxy for GPP of corn and soybean. Environmental Research Letters, 15(3): 034009,https://doi.org/10.1088/1748-9326/ab65cc.

Zeng, Y. et al., 2019. A practical approach for estimating the escape ratio of near-infrared solar-induced chlorophyll fluorescence. Remote Sensing of Environment, 232: 111209,https://doi.org/10.1016/j.rse.2019.05.028.

Zhang, H. et al., 2021. Retrieving high-resolution surface photosynthetically active radiation from the MODIS and GOES-16 ABI data. Remote Sensing of Environment, 260: 112436,https://doi.org/10.1016/j.rse.2021.112436.

Zhang, Y. et al., 2018. On the relationship between sub-daily instantaneous and daily total gross primary production: Implications for interpreting satellite-based SIF retrievals. Remote Sensing of Environment, 205: 276-289,https://doi.org/10.1016/j.rse.2017.12.009.

Zhang, Z. et al., 2020. Reduction of structural impacts and distinction of photosynthetic pathways in a global estimation of GPP from space-borne solar-induced chlorophyll fluorescence. Remote Sensing of Environment, 240: 111722,https://doi.org/10.1016/j.rse.2020.111722.

Zhu, X., Cai, F., Tian, J. and Williams, T.K.-A., 2018. Spatiotemporal Fusion of Multisource Remote Sensing Data: Literature Survey, Taxonomy, Principles, Applications, and Future Directions. Remote Sensing, 10(4): 527,https://doi.org/doi:10.3390/rs10040527.

Supplementary Materials

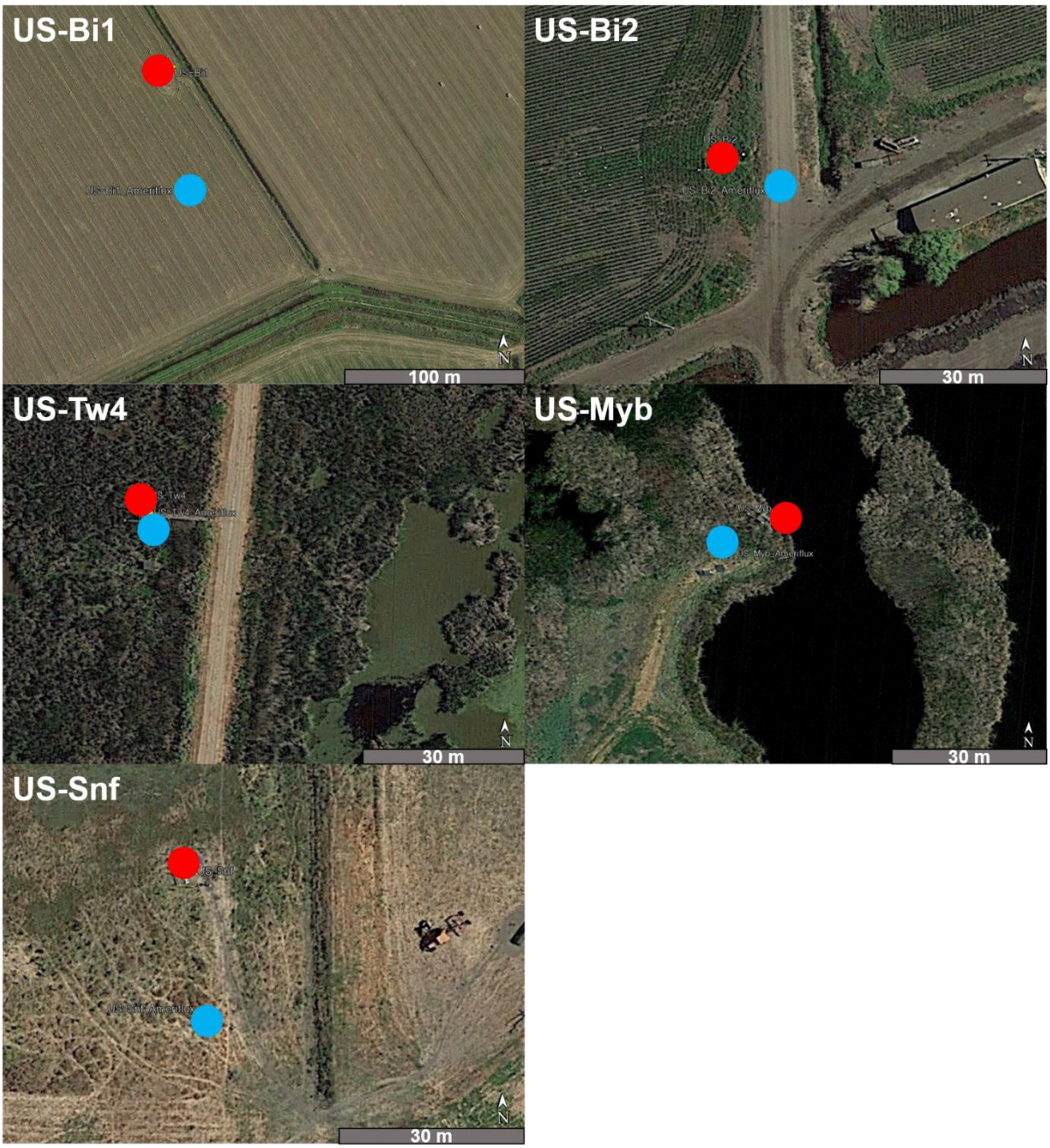

Figure S1 Location of fluxtower: registered in Ameriflux (Blue) and corrected location in this study (Red) over the study sites (Image source: Google Earth).

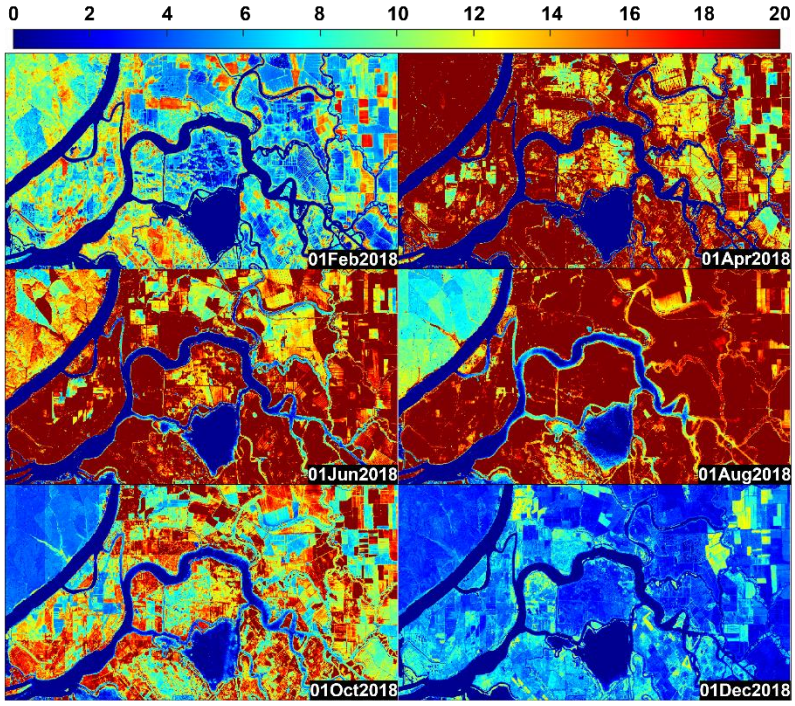

Figure S2 Maps of NIRvP derived from the combined Planet Fusion surface reflectance product and BESS daily PAR product throughout 2018 (projection, WGS84/UTM zone 10N; area, 30.6 km × 14.2 km = 433 km^2). NIRvP is given in unit of mol m^{-2} d^{-1}.

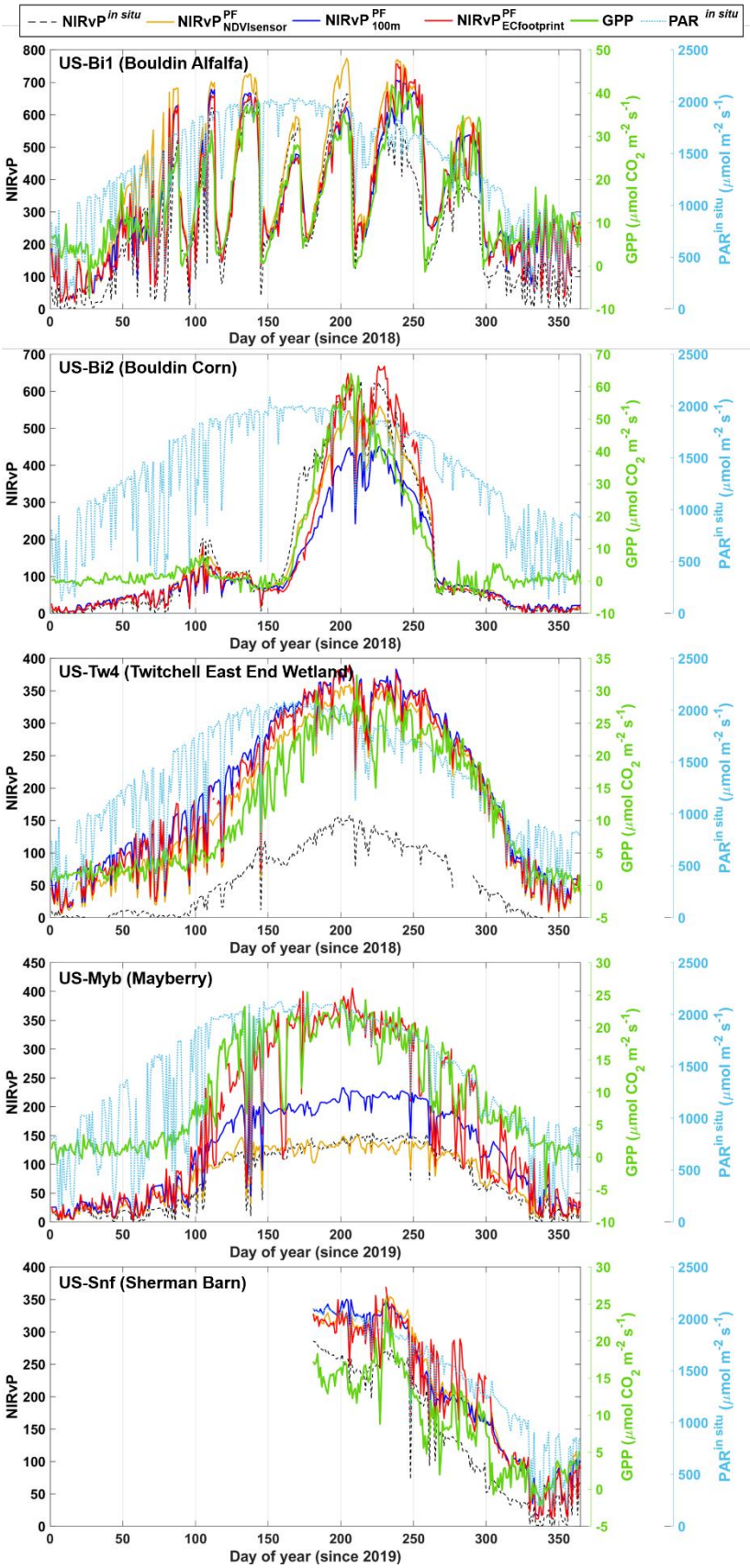

Figure S3 Seasonal variation of NIRvP from *in situ* and Planet Fusion (PF) in different footprint types (left axis), that of GPP (right axis; green), and *in situ* PAR (right axis; blue) around satellite passing time. NIRvP is given in unit of μmol m^{-2} s^{-1}.

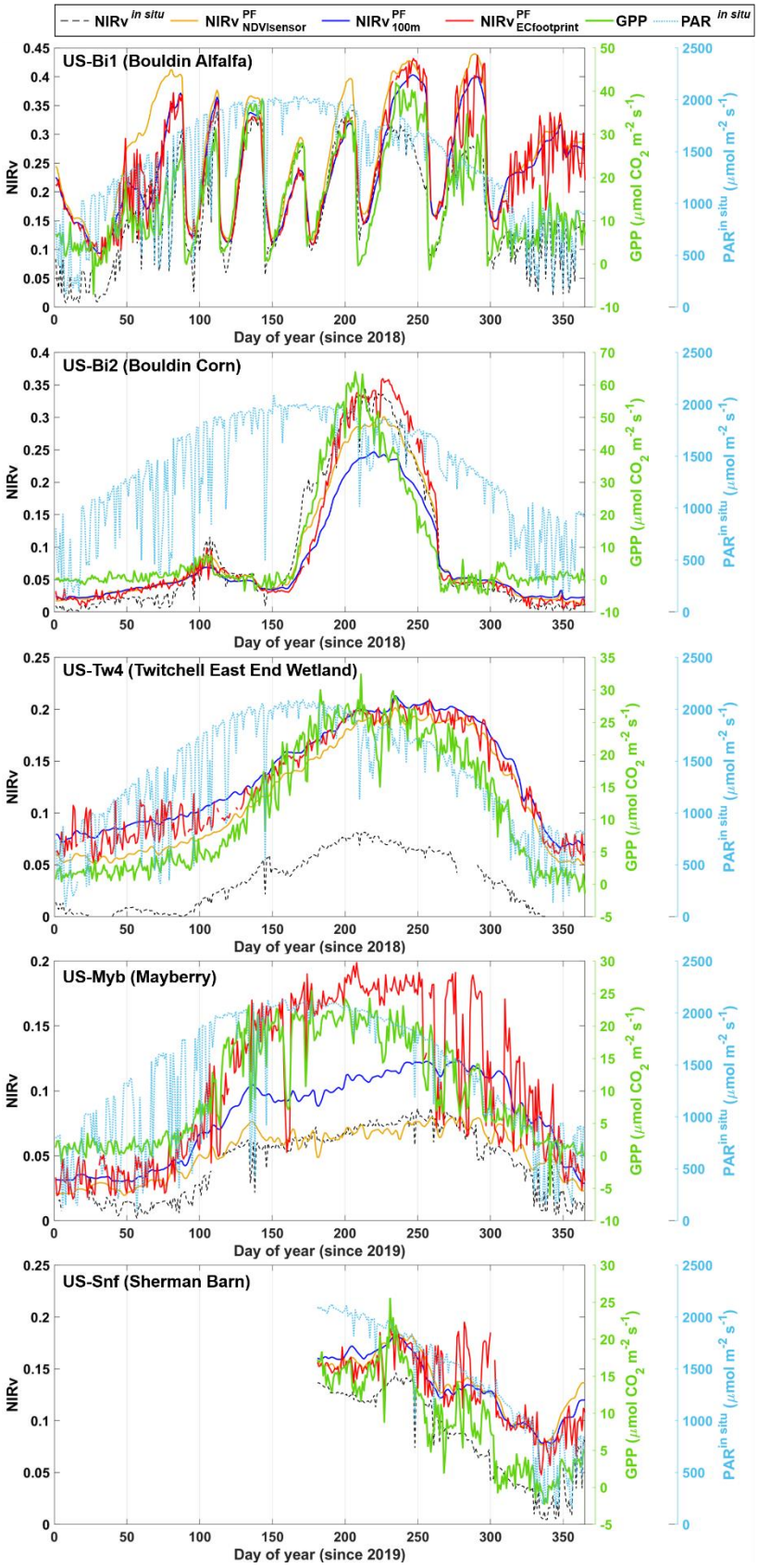

Figure S4 Seasonal variation of NIRv from *in situ* and Planet Fusion (PF) in different footprint types (left axis), that of GPP (right axis; green), and *in situ* PAR (right axis; blue) around satellite passing time. NIRv is given in unitless.

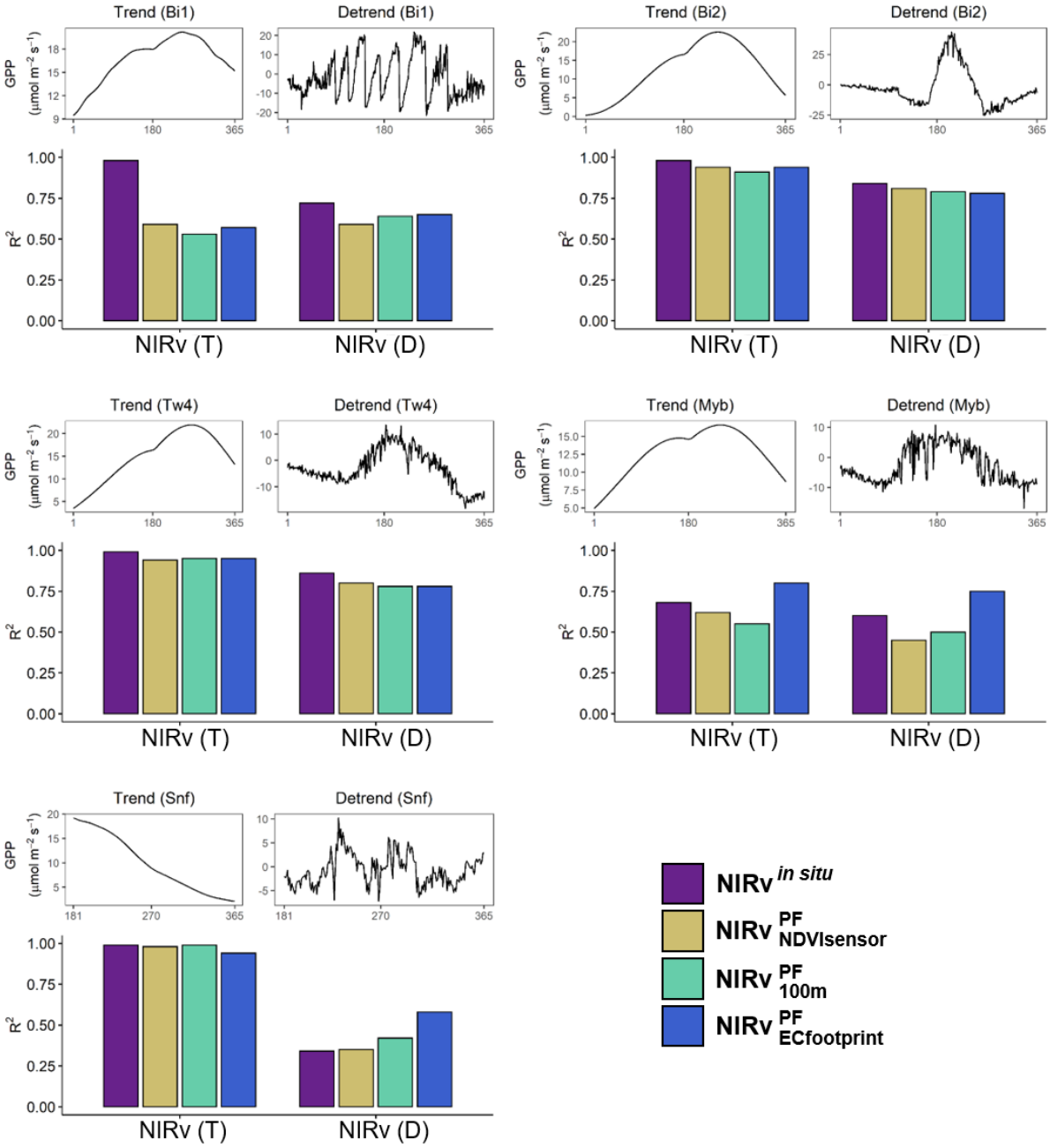

Figure S5 The GPP trend (T) and detrended (D) GPP at each site. Linear relationships of gap-filled Planet Fusion (PF) NIRv and *in situ* NIRv with T and D at the satellite passing time are also shown. $NIRv^{PF}_{NDVIsensor}$, $NIRv^{PF}_{100m}$, $NIRv^{PF}_{ECfootprint}$ denotes Planet Fusion -derived NIRv around the local satellite overpassing time in different footprint type (i.e., $NDVI_{sensor}$, 100m, and $EC_{footprint}$). Detailed site data for the entire study period are shown in (Figure S4).

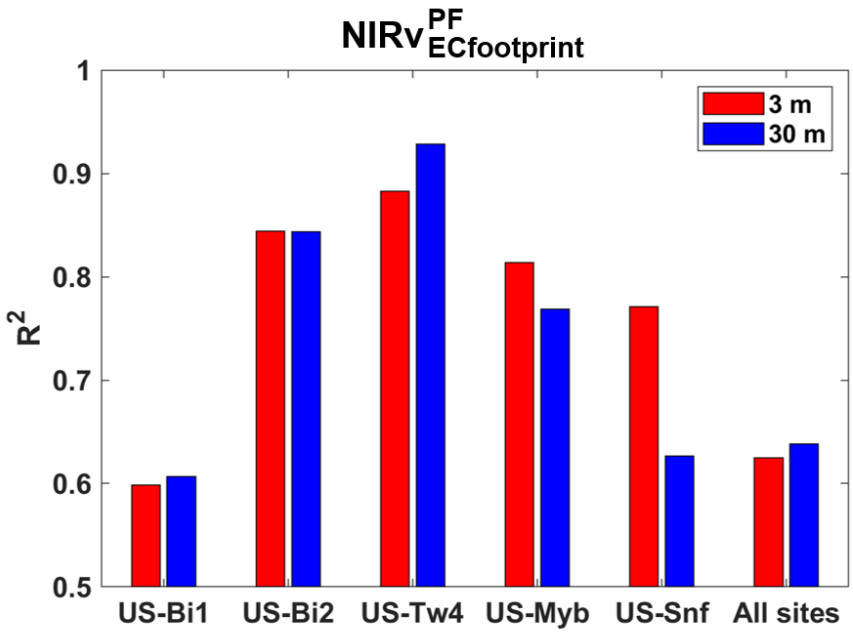

Figure S6 Evaluation of Planet Fusion (PF) derived NIRv within eddy covariance (EC) footprint in different spatial resolution against GPP around satellite passing time. $NIRv^{PF}_{ECfootprint}$ denotes Planet Fusion-derived NIRv in daily eddy covariance footprints at the local satellite overpassing time. The linear relationships against GPP are shown. The detailed numbers are in (Table A6).

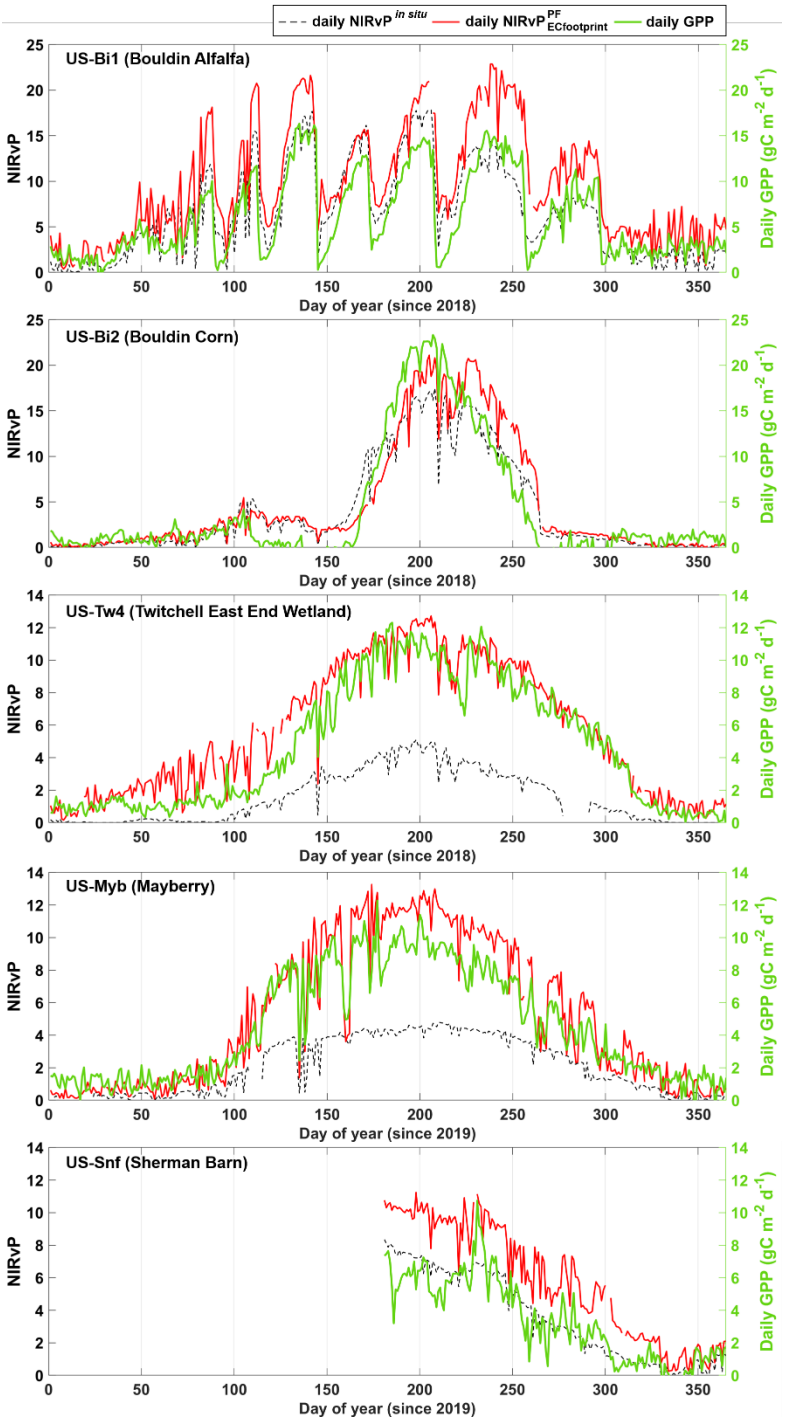

Figure S7 Seasonal variation of daily NIRvP from *in situ* and Planet Fusion (PF) in different footprint types (left axis) and that of daily GPP (right axis). NIRvP is given in unit of mol m^{-2} d^{-1}.

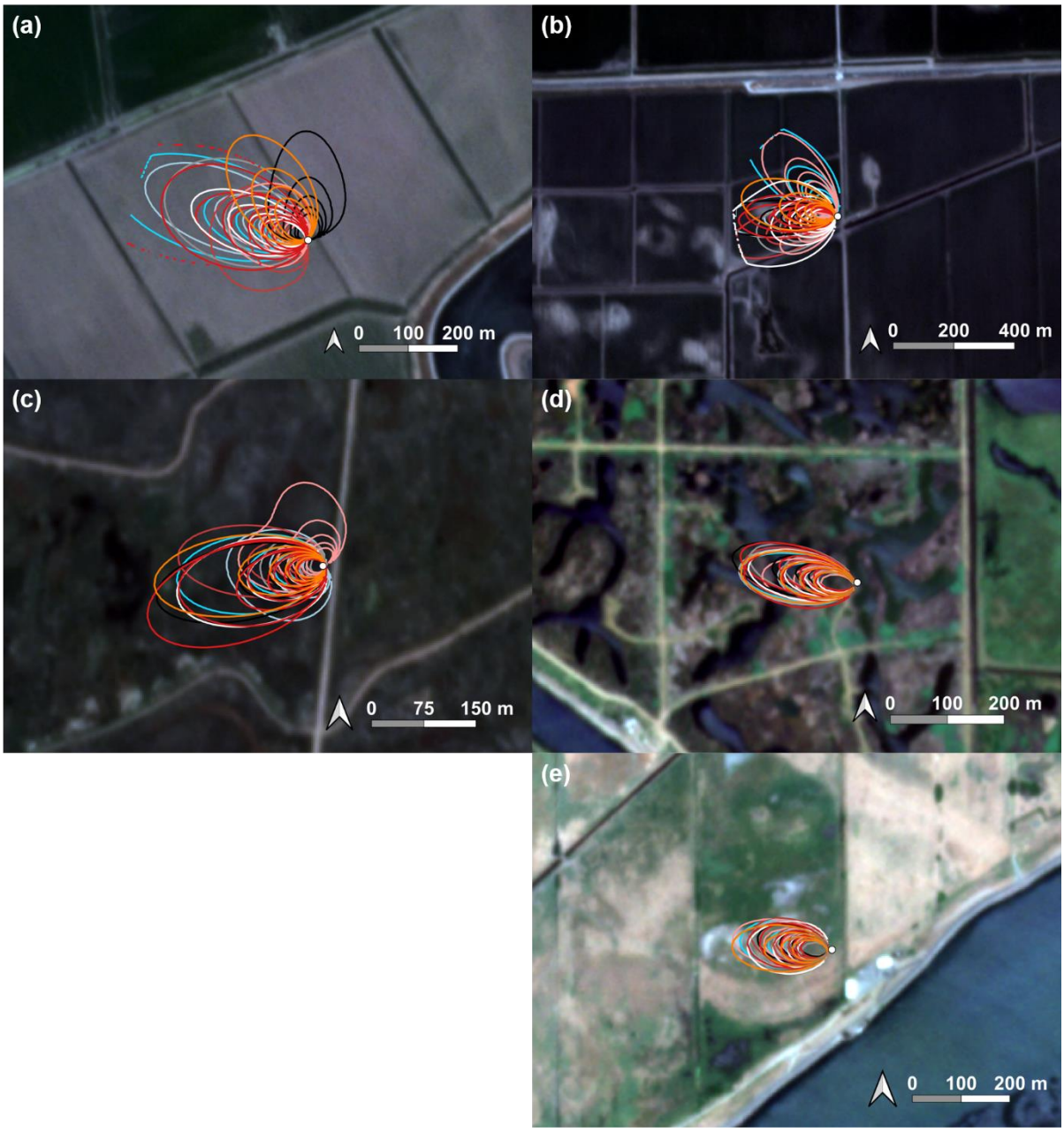

Figure S8 Examples of daily eddy covariance (EC) footprints at sites (a) US-Bi1 (Alfalfa), (b) US-Bi2 (Corn), (c) US-Tw4 (Freshwater wetland), (d) US-Myb (Palustrine wetland), and (e) US-Snf (Pasture) from July 1–10 (colored lines at each date), 2018 (a-c) and 2019 (d-e). Contour lines delineate footprints within which (a–c) 50–90% and (d) 50–80% of the cumulative flux originated. Image source: red–green–black (RGB) Planet Fusion surface reflectance product (projection, WGS84/UTM zone 10N) for (a–c) July 1, 2018, and (d-e) July 1, 2019.

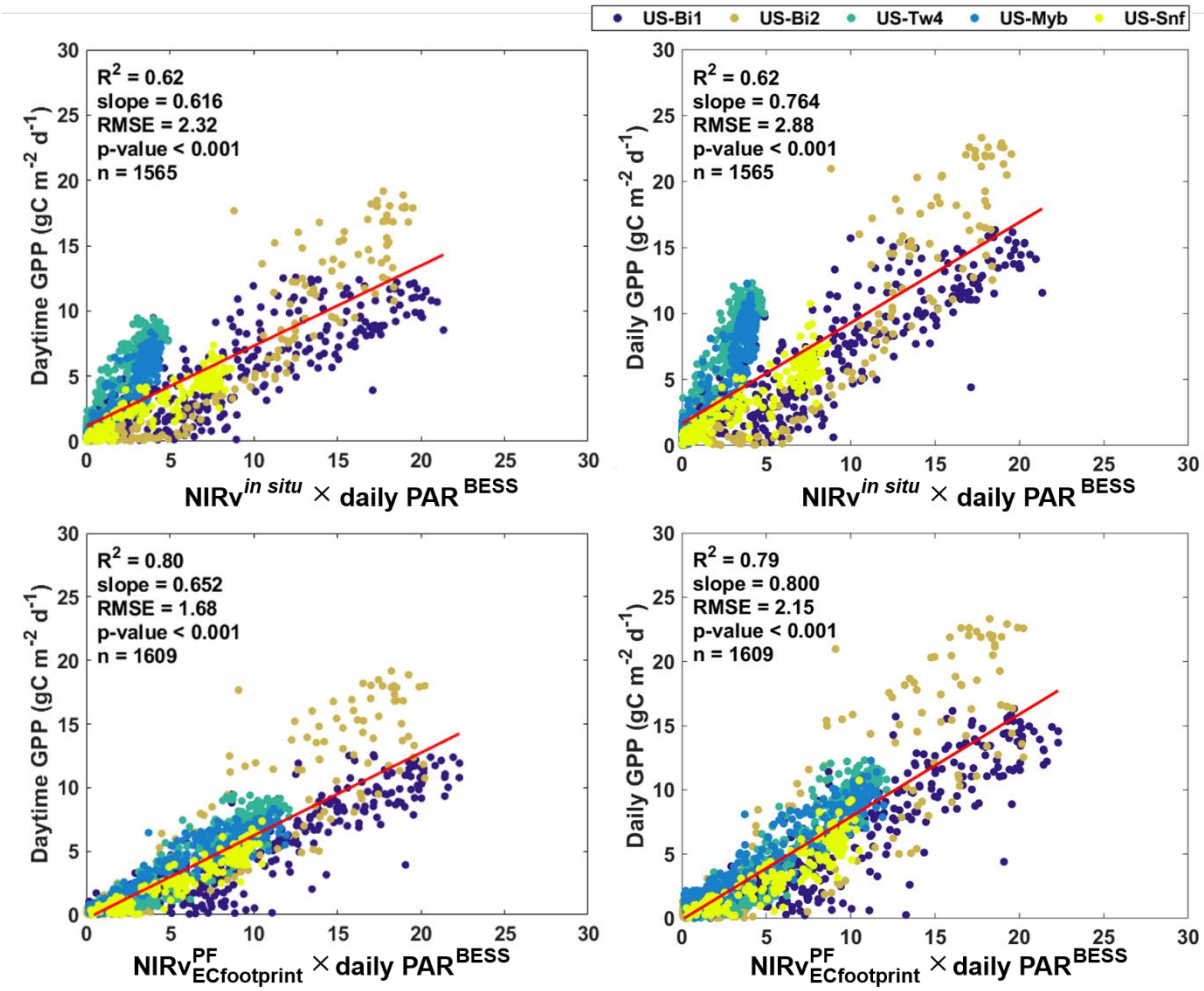

Figure S9 Linear relationships between *in situ*-measured and Planet Fusion (PF)-derived daily NIRvP and daily GPP at all sites (colored circles). Daily GPP is the whole day (0000hh – 2400hh) summed value and Daytime GPP is daytime (0800hh-1800hh) summed value. daily PAR^{BESS} means daily summed PAR data retrieved from the satellite-based Breathing Earth System Simulator (BESS). Red line indicates the linear regression model slope of overall sites. R^2 is the coefficient of determination, p-value indicates the significance of the linear regression, and n is the number of samples used in the linear regression model. NIRvP is given in unit of mol m^{-2} d^{-1}.